AAPM REPORT NO. 195

Monte Carlo Reference Data Sets for Imaging Research

The Report of AAPM Task Group 195

September 2015

DISCLAIMER: This publication is based on sources and information believed to be reliable, but the AAPM, the authors, and the editors disclaim any warranty or liability based on or relating to the contents of this publication.

The AAPM does not endorse any products, manufacturers, or suppliers. Nothing in this publication should be interpreted as implying such endorsement.

This page intentionally left blank.

Monte Carlo Reference Data Sets for Imaging Research

The Report of AAPM Task Group 195

Ioannis Sechopoulos[1*] (chair), Elsayed S. M. Ali[2**], Andreu Badal[3], Aldo Badano[4], John M. Boone[5], Iacovos S. Kyprianou[6], Ernesto Mainegra-Hing[7], Michael F. McNitt-Gray[8], Kyle L. McMillan[9], D. W. O. Rogers[10], Ehsan Samei[11], and Adam C. Turner[12***]

[1]Emory University, Atlanta, Georgia, USA
[2,10]Carleton University, Ottawa, Ontario, Canada
[3,4,6]Food and Drug Administration, Rockville, Maryland, USA
[5]University of California, Davis, California, USA
[7]National Research Council Canada, Ottawa, Ontario, Canada
[8,9,12]University of California, Los Angeles, California, USA
[11]Duke University, Durham, North Carolina, USA

*Present address: Radboud University Medical Center and the Dutch Reference Centre for Screening (LRCB)
**Present address: The Ottawa Hospital Cancer Centre
***Present address: Ironwood Cancer and Research Centers

ISBN: 978-1-936366-38-5
ISSN: 0271-7344

Published by

American Association of Physicists in Medicine
One Physics Ellipse
College Park, MD 20740-3846

Contents

Abstract

The use of Monte Carlo simulations in diagnostic medical imaging research is widespread due to its flexibility and ability to estimate quantities that are challenging to measure empirically. However, any new Monte Carlo simulation code needs to be validated before it can be used reliably. The type and degree of validation required depends on the goals of the research project, but typically, such validation involves either comparison of simulation results to physical measurements or to previously published results obtained with established Monte Carlo codes. The former is complicated due to nuances of experimental conditions and uncertainty, while the latter is challenging due to typical graphical presentation and lack of simulation details in previous publications. In addition, entering the field of Monte Carlo simulations in general involves a steep learning curve. It is not a simple task to learn how to program and interpret a Monte Carlo simulation, even when using one of the publicly available code packages. This task group report provides a common reference for benchmarking Monte Carlo simulations across a range of Monte Carlo codes and simulation scenarios. All simulation conditions are provided for six different Monte Carlo simulation cases that involve common x-ray-based imaging research areas. For all cases, the results obtained with four publicly available Monte Carlo software packages are included in tabular form. In addition to a full description of all simulation conditions and results, a discussion and comparison of results among the Monte Carlo packages and the lessons learned during the compilation of these results are included.

This work provides an investigator the necessary information to benchmark his/her Monte Carlo simulation software against the reference cases included here before performing his/her own novel research. In addition, an investigator entering the field of Monte Carlo simulations can use these descriptions and results as a self-teaching tool to ensure that he/she is able to perform a specific simulation correctly. Finally, educators can assign these cases as learning projects as part of course objectives or training programs.

1. INTRODUCTION

The use of Monte Carlo methods in diagnostic medical imaging research is an attractive option because of the relative ease with which many different calculations can be performed. These simulations sometimes span large parameter spaces or obtain estimates of quantities that are not simple to measure empirically, e.g., absorbed dose or x-ray scatter. The ever-continuing reduction in the cost of computing power has also helped increase the use of this research methodology.

As with all other types of experimentation, Monte Carlo simulations need to be validated before their results can be trusted. In many cases, the validation process for a Monte Carlo simulation is not a simple endeavor. Ideally, Monte Carlo-based computer programs are validated by generating a simulation that replicates an empirical test and then comparing simulation and empirical results. However, this requires replicating the conditions of a physical experiment to a high level of accuracy and detail in the computer simulation to minimize differences from the measurement conditions. This level of replication of a physical experiment can be extremely challenging, even for simple experimental conditions.

One possible step in the validation process of Monte Carlo simulations is the replication of published (and previously validated) simulations. However, this approach also presents challenges. In the first place, a relevant previously published simulation has to exist. Once one is identified, a common pitfall is the lack of sufficient detail in the description of the simulation, making its replication extremely challenging. In addition, many times the published results are provided in graphs or summarized form, so an appropriate comparison with the results of the simulation being validated can be limited and the effort laborious.

To aid researchers in their efforts to validate their Monte Carlo simulations in imaging research or to assist in the validation process of their use of a general purpose code already available, this report provides six different reference sets of simulations that include a complete description of the simulation conditions. In addition, the simulation results for all sets—as generated by four commonly used Monte Carlo packages—are provided in tabulated form along with their statistical uncertainty. These data sets allow the reader to accurately replicate the geometry, source properties, and scoring. In this way, the reader can have confidence that his/her simulation is providing accurate results against these thoroughly vetted reference cases. The agreement amongst the four codes used here indicates the level of accuracy to be expected as these codes have all been benchmarked against experimental data in different situations.[1–10] It is worth to emphasize that as our results were not based on experimental measurements, the validation achieved through this benchmarking is only relative to these calculations with widely used codes and not directly to measurements. But the concordance between the four Monte Carlo results provides strong confidence for the value and the validity of this exercise. It is in that sense that we use the term “validation” throughout the body of this document. In publications and presentations involving the code, a reference to this report and the obtained level of agreement will be sufficient to communicate the performance of this component of a validation effort.

Another factor often complicating Monte Carlo simulations is the fact that learning to perform these simulations involves a steep learning curve. It takes a substantial amount of time and effort to become comfortable in the programming method for using any of the publicly available Monte Carlo packages. To help address this, it is hoped that these reference simulation sets can also be used as a teaching tool, either for a scientist entering the field of Monte Carlo simulations in diagnostic imaging, or for a supervising educator training students or junior researchers in the field. The availability of the complete descriptions of relevant simulations and their expected results when using different well-established Monte Carlo codes may be used to check one’s own skills or as an assignment for trainees.

The diagnostic imaging simulation sets included in this report are listed in Table 1. They span a number of x-ray-based imaging modalities and common quantities scored with Monte Carlo simula-

Table 1: List of the simulations sets included in this report

Case Number	Modality/Description	Quantities Scored
1	Half Value Layer	Fluence
2	Radiography and Body Tomosynthesis	(a) Total dose (b) X-ray primary and scatter photon energy
3	Mammography and Breast Tomosynthesis	(a) Total dose and glandular dose (b) X-ray primary and scatter photon energy
4	Computed Tomography (simple volumes)	Dose
5*	Computed Tomography (voxelized volumes)	Dose
6	X-ray Production	Photon energy fluence and fluence spectra

* Case 5 may also be useful for dosimetry simulations with other imaging modalities (e.g., radiography, body tomosynthesis) that involve voxelized models of patients.

tions. While this is a limited set that does not encompass all modalities and tests that are commonly investigated using Monte Carlo methods, the defined conditions provide a meaningful representation of Monte Carlo-based research. Future reports might be generated to provide additional reference data sets involving other imaging modalities (e.g., nuclear medicine) or simulation conditions (e.g., detector simulations).

This report is organized as follows. In Section 2, a description of all the parameters common to the simulation sets is provided. This includes the Monte Carlo packages used to generate the results and the material compositions and x-ray spectra used throughout the simulation sets. Section 3 provides a description of each simulation with all the details necessary to replicate it. Section 4 provides the results obtained by the task group members for each simulation set. Section 5 includes a discussion on the common pitfalls encountered in the implementation of the simulations ("lessons learned") and a discussion on the differences in the results obtained with the Monte Carlo packages used in this report. Finally, the Appendix provides the Monte Carlo package-specific parameters used by the task group members to perform the Monte Carlo simulations used to generate the results included in this report.

2. COMMON PARAMETERS

2.1 Monte Carlo Packages

All simulation conditions described in this report were implemented with four commonly used and well-established Monte Carlo packages (Table 2). Results from all four implementations of each simulation are provided in this report. These packages were selected for inclusion in this report due to their being commonly used by the diagnostic imaging research community, their availability and continued development and maintenance, and the expertise of the task group members in using them. Inclusion of these Monte Carlo packages in this report should not be interpreted as any form of endorsement by the task group or the American Association of Physicists in Medicine (AAPM), and the exclusion of any other Monte Carlo package should not be interpreted as disapproval by the same.

It should be noted that the results and performance of the four Monte Carlo packages used for this report should not be necessarily construed to be the best achievable with each package. The results and performance obtained with these packages reflect the best attempts of the task group members to match the conditions specified in each case description, with logical choices for each code-specific parameter. The simulations were not necessarily optimized for minimizing running time or to achieve the maximum level of accuracy beyond that of typical use. In addition, errors could have been made during the implementation of the simulations.

Table 2: Monte Carlo packages used to generate the results included in this report, in alphabetical order

Package Name	Version	Photon Cross Sections	References	Comments
EGSnrc	V4 r2.4.0	EGSnrc default (XCOM: Rayleigh, photoelectric and pair production. RIA: Incoherent scattering.)	11–14	Used in all cases except for Case 1, where NIST XCOM cross sections were used for all interactions.
Geant4	9.6 patch 2	Electromagnetic physics option 4 package	15,16	Used in all cases except for Case 6, where the Livermore electromagnetic physics were used.
MCNPX	2.7a	ENDF/B-VII	17	Used in all cases.
Penelope	2006	Penelope default (XCOM and EPDL)	18–20	Used in all cases except Case 6. Used with the penEasy main program adapted for parallel simulation with MPI library.
	2008	Penelope default (XCOM and EPDL)		Used in Case 6, with standard penEasy main program.

2.2 Simulated Material Compositions

The composition of materials used in all simulations is provided in two separate electronic files available for download in the electronic resources included with this report. One file includes all material compositions for all cases, except those used in Case #5, which are defined in a separate file.

The densities specified for the elements, as well as the material composition for the simpler compounds, were those provided by the National Institute of Standards and Technology (NIST).[21] The composition of soft tissue used is that provided by the International Commission on Radiation Units and Measurements (ICRU).[22] Due to their common use in breast imaging research, the material compositions related to mammography and breast tomosynthesis are those provided by Hammerstein et al.[23]

2.3 X-ray Spectra

The probability distribution functions of the x-ray spectra used as inputs in the simulations included in this report were obtained using Report 78 of the Institute of Physics and Engineering in Medicine (IPEM).[24] They were defined so as to approximate certain x-ray spectra defined in Publication 61267 of the International Electrotechnical Commission.[25] The spectra definitions do not comply with the IEC 61267 requirement for their homogeneity coefficient, the ratio of the first to the second half value layer, however all other requirements are met, and this has no effect on the validity of this benchmarking process. Table 3 lists the x-ray spectra used and the parameters specified for the generation of their distribution functions using the IPEM Report 78 software. The resulting spectra are plotted in Figure 1. The distribution functions themselves are available for download in the electronic resources included with this report.

The energy bin width for all spectra is 0.5 keV, starting at 0 keV, and the energy of the center of the bin is listed. During the Monte Carlo simulations, the provided distribution functions should be sampled uniformly within each bin.

Table 3: Characteristics of x-ray spectra used for the simulations included in this report. All x-ray spectra are described with probability distribution functions with bin width of 0.5 keV starting at 0 keV. The mid-bin energy of the bins is listed in the electronic resource file with the probability distribution functions. HVL and QVL values are in terms of air kerma determined using planar fluence.

Characteristics	IEC 61267 Name		
	RQR-8	**RQR-9**	**RQR-M3**
Target/Filter Elements	W/Al	W/Al	Mo/Mo
Tube Voltage (kVp)	100	120	30
Anode Angle (deg)	11	11	15
Ripple (%)	0	0	0
Filter Thickness (mm)	2.708	2.861	0.0386
Mean Energy (keV)	50.6	56.4	16.8
Half Value Layer (HVL) (mm Al)*	3.950	5.010	0.3431
Quarter Value Layer (QVL) (mm Al)†	9.840	–	0.7663

* These values are not those reported by IPEM Report 78 software, but were calculated by the task group using the NIST XCOM dataset.[21]
† Provided for the two spectra used in Case #1 only.

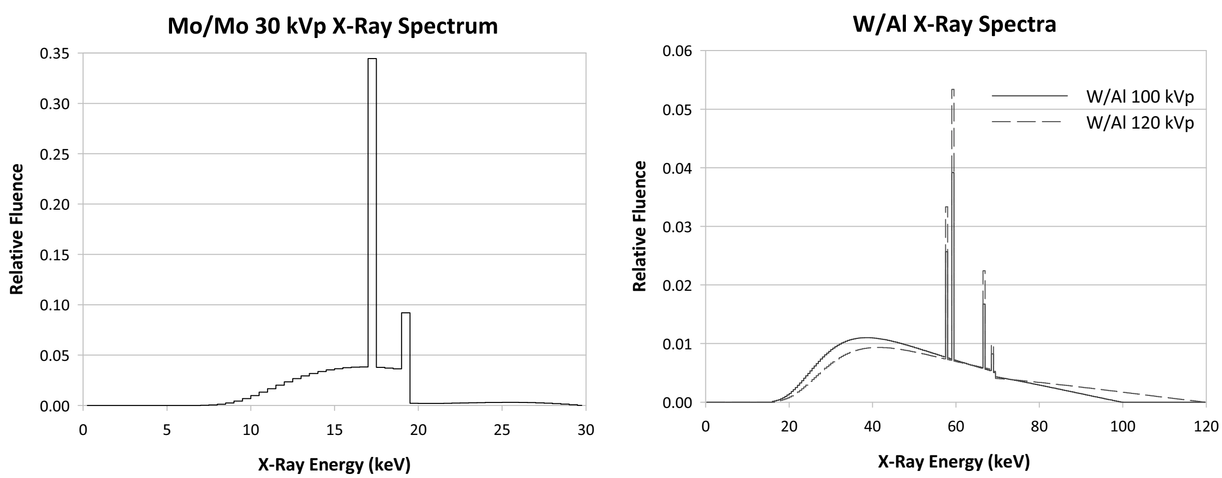

Figure 1. Graphs of the x-ray spectra, normalized to unit fluence under the curve, used in the Monte Carlo simulations included in this report.

3. SIMULATION DESCRIPTIONS

This section provides the complete description of the simulations with all details necessary to replicate the conditions used in the implementation of each by the task group. All references to materials and x-ray spectra refer to those defined in Section 2 and as provided in the electronic resources.

3.1 Case 1: Half Value Layer

Aim

This case aims to verify the accuracy of input x-ray spectrum sampling, basic material attenuation, and half-value layer calculations.

Geometry

1. Filter is a disk of thickness **t** mm and diameter 40 mm (Figure 2). The central axis of the filter coincides with the +z axis. The superior face of the filter is 100 mm below the source.
2. Simulations are performed for two thicknesses (**t**), corresponding to the theoretical half-value layer (HVL) and quarter value layer (QVL), respectively, as given in Table 4 (also listed in Table 3 with the description of the x-ray spectra).

Materials

Filter material is aluminum and the rest of the geometry is filled with air.

Radiation Source

1. Radiation source is an isotropic x-ray point source at the geometry origin (x=0, y=0, z=0), collimated to a central circle of 1 mm diameter at the superior face of the filter.
2. Simulations are performed for monoenergetic photons and for spectra as given in Table 4.

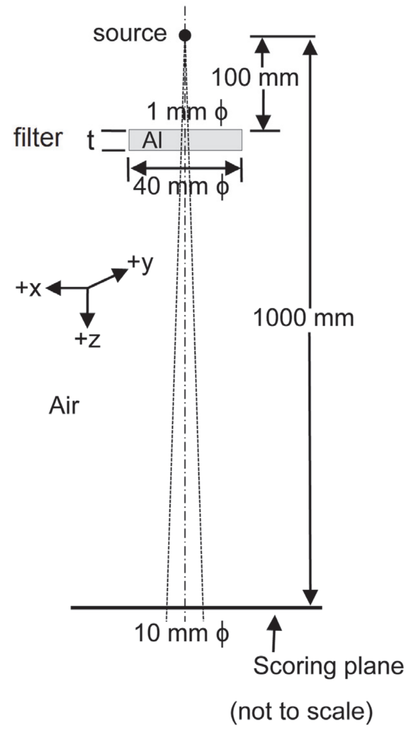

Figure 2. Diagram of the geometry setup for Case #1.

Scoring

1. Scoring is performed in a central circle of 10-mm diameter at the plane z = +1000 mm without the presence of the filter and with the filters set at the two thicknesses specified in Table 4.
2. By planar energy fluence it is meant $\psi = \sum_i (E_i)/A$, where E_i is the energy of the incident x-ray and A is the area, without consideration for the cosine of the incidence angle.
3. For monoenergetic photons, the quantities scored are as follows:
   a. Primary (non-scattered) planar energy fluence ($\psi_p(t)$) at the incident photon energy.
   b. Scatter ($\psi_s(E, t)$) differential planar energy fluence, binned in 0.5 keV bins between zero and the incident photon energy, to match the bin resolution of the input spectra.

Table 4: Simulation parameters for Case #1

X-ray Energy/Spectrum	t for Theoretical HVL (mm Al)	t for Theoretical QVL (mm Al)
30 keV	2.273	4.546
100 keV	15.11	30.22
Mo/Mo 30 kVp	0.3431	0.7663
W/Al 100 kVp	3.950	9.840

4. For x-ray spectra, the quantities scored are the primary ($\psi_{\mathbf{p}}(E, t)$) and scatter ($\psi_{\mathbf{s}}(E, t)$) differential planar energy fluences using the same bin definitions as above.
5. All planar energy fluence values are converted to air kerma (AK) off-line, using the air mass energy absorption coefficients, $\left(\frac{\mu_{en}}{\rho}\right)$, available for download in the electronic resources included with this report on a 0.5 keV spacing, as obtained from NIST,[21] and the following equation:

$$AK = E\Phi\left(\frac{\mu_{en}}{\rho}\right) \tag{3.1}$$

where E is the mid-point energy bin of the incident x-ray and Φ is the planar fluence at energy bin E.

Since this conversion is done off-line using the provided coefficients, all energy fluence for each bin is assumed to be at the mid energy of the bin. As can be seen in the provided electronic file, all mass energy absorption coefficients for x-ray energies below 3.75 keV are listed as zero, so any incident photons below this energy may be ignored.
6. Final results are the following four air kerma ratios for each x-ray source energy definition:
   a. Primary only, resulting AK ratio after HVL:

$$R_1 = \frac{\sum_E AK_p(E,\ t = HVL)}{\sum_E AK_p(E,\ t = 0)} \tag{3.2}$$

   b. Primary only, resulting AK ratio after QVL:

$$R_2 = \frac{\sum_E AK_p(E,\ t = QVL)}{\sum_E AK_p(E,\ t = 0)} \tag{3.3}$$

   c. Primary and scatter, resulting AK ratio after HVL:

$$R_3 = \frac{\sum_E AK_p(E,\ t = HVL) + \sum_E AK_s(E,\ t = HVL)}{\sum_E AK_p(E,\ t = 0) + \sum_E AK_s(E,\ t = 0)} \tag{3.4}$$

   d. Primary and scatter, resulting AK ratio after HVL:

$$R_4 = \frac{\sum_E AK_p(E,\ t = QVL) + \sum_E AK_s(E,\ t = QVL)}{\sum_E AK_p(E,\ t = 0) + \sum_E AK_s(E,\ t = 0)} \tag{3.5}$$

Statistical Uncertainty

The number of simulated x-rays is such that the statistical uncertainty is 1% or lower on the primary total planar energy fluence in the case of monoenergetic incident photons, and 1% on the primary differential planar energy fluence in any given bin in the case of incident spectra.

3.2 Case 2: Radiography and Body Tomosynthesis

Aim

This case aims to verify the accuracy of x-ray transport and interaction characteristics in general radiography and whole body tomosynthesis simulations. It scores absorbed dose in the body and the energy of both x-ray primary and scatter components incident upon the detection plane. Depending on the application, the dosimetry or the fluence component results may be tested.

Geometry

1. Body is a box of thickness (z-direction) 200 mm, with width (x-direction) and height (y-direction) 390 mm. Its center is located at the x-y coordinates (0, 0) and its entrance surface is 1550 mm from the x-ray source (figures 3 and 4).

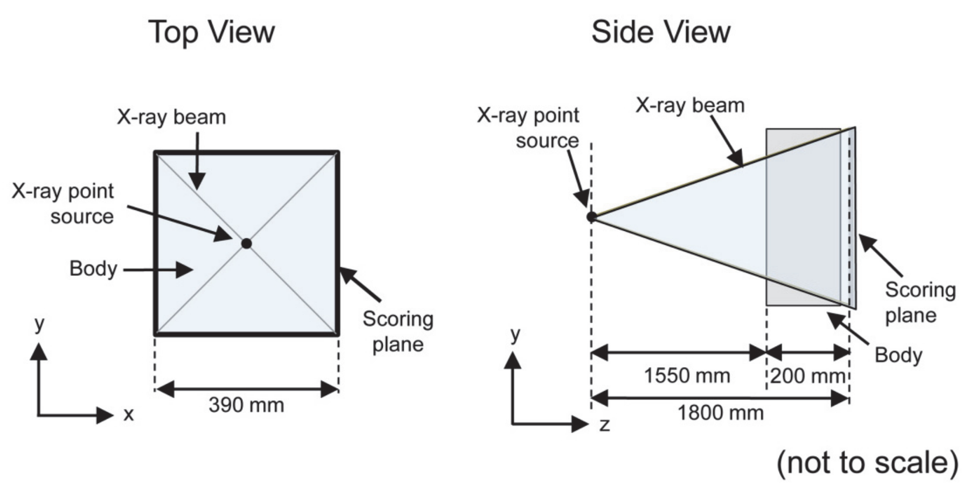

Figure 3. Diagram of the geometry setup for Case #2 with the x-ray source positioned for the radiography acquisition (equivalent to the tomosynthesis 0° angle).

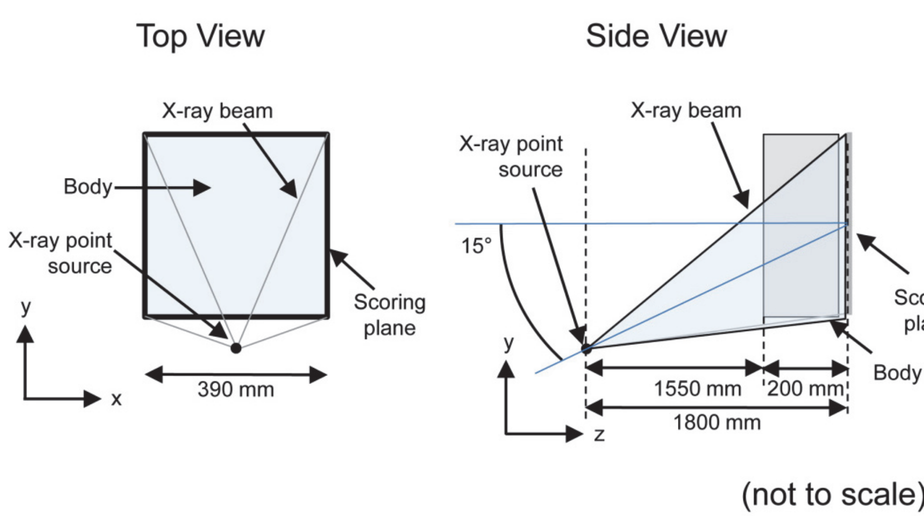

Figure 4. Diagram of the geometry setup for Case #2 with the x-ray source positioned for the tomosynthesis 15° angle acquisition.

2. Scoring plane has 390 mm sides in the x-y directions and is located 50 mm past the body.

Materials

Body material is soft tissue, and the rest of the geometry is filled with air.

Radiation Source

1. Radiation source positions are as follows:
    a. For simulation of radiography and a 0° tomosynthesis projection, source is located at the geometry origin (x=0, y=0, z=0).
    b. For simulation of the 15° tomosynthesis projection, source is displaced along the –y direction, forming an angle of 15° with the scoring plane.
    c. These positions apply to both the full field and the point spread function simulations.
2. For validation of dosimetry, the x-ray source is an isotropic point source with the x-ray beam collimated electronically for congruence with all four edges of the scoring plane.
3. For validation of x-ray scatter, two types of sources are used:
    a. First test (full field): Same as point 2 above for validation of dosimetry.
    b. Second test (point-spread function): X-ray point source emits a zero-area beam aimed at the center of the scoring plane.
4. Simulations are performed for the W/Al 120 kVp spectrum and for monoenergetic photons with energy 56.4 keV (equivalent to the mean energy of the spectrum).

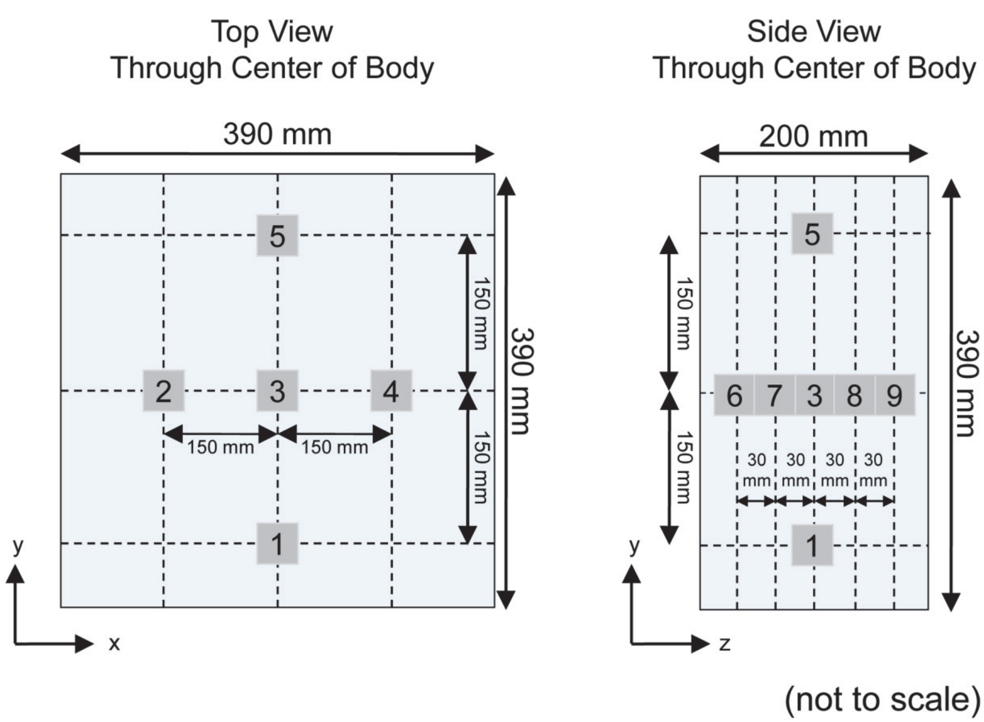

Figure 5. Diagram showing the locations of the VOIs within the simulated body of Case #2 where the energy deposition is scored for validation of the dosimetry simulation. VOI 3 is located at the center of the body in all three directions. VOIs 1, 2, 4, and 5 are at the same z location as VOI 3. VOIs 1, 5, 6, 7, 8, and 9 are at the same x location as VOI 3.

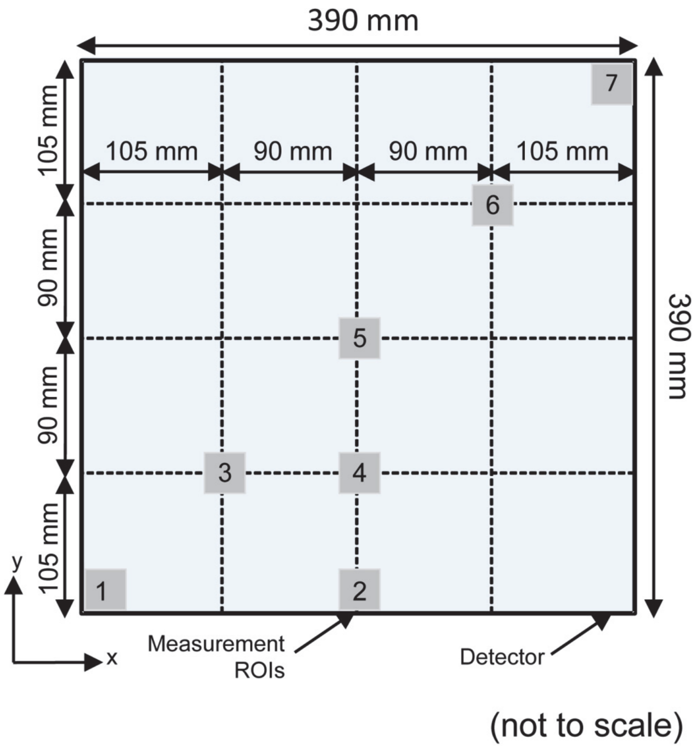

Figure 6. Diagram showing the locations of the ROIs within the scoring plane of Case #2 where the incident primary and scatter energy is scored for validation of the x-ray scatter simulation with a full-field x-ray beam. ROI 5 is located at the center of the scoring plane.

Scoring

1. For validation of dosimetry, two sets of scoring results are provided:
   a. Total energy deposited in the body per initial photon.
   b. Energy deposited in 9 cubic volumes of interest (VOIs) inside the body per initial photon, each is 27,000 mm^3 (30 mm × 30 mm × 30 mm). Five VOIs are located on the central plane parallel to the scoring plane. Four additional VOIs are located on the central axis perpendicular to the scoring plane. The locations are shown in Figure 5.
2. When validating x-ray primary and scatter components for the first test using a full-field x-ray beam, the scoring is as follows:
   a. Primary x-ray energy per initial photon, incident on the 7 regions of interest (ROIs), each 30 mm × 30 mm, throughout the scoring plane, according to Figure 6.
   b. Scatter x-ray energy per initial photon, incident on the same 7 ROIs.

   These ROIs correspond to 30 mm × 30 mm regions with the following image indices:

   1: (0, 0)

   2: (6, 0)

   3: (3, 3)

   4: (6, 3)

5: (6, 6)

6: (9, 9)

7: (12, 12)

3. When validating x-ray scatter for the second test using a zero-area beam resulting in a point-spread function, the scoring should be as follows:
   a. Incident scatter x-ray energy per initial photon, at 7 ROIs, each 30 mm × 30 mm, throughout the scoring plane, according to Figure 7.
   b. Incident primary x-ray energy per initial photon, at ROI 5, according to Figure 7.

   These ROIs correspond to 30 mm × 30 mm regions with the following image indices:

   1: (4, 4)

   2: (6, 4)

   3: (5, 5)

   4: (6, 5)

   5: (6, 6)

   6: (7, 7)

   7: (8, 8)

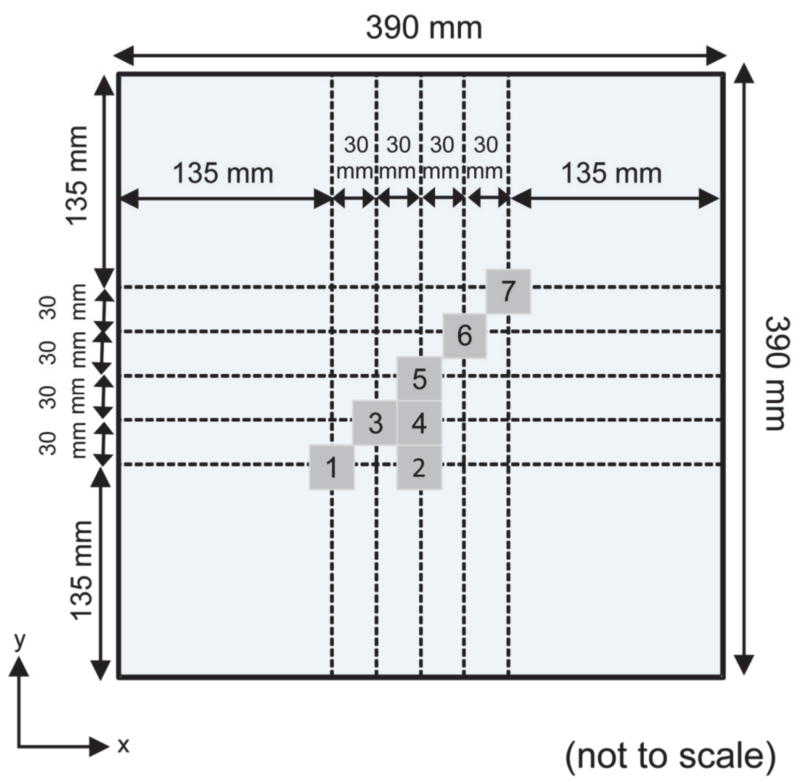

Figure 7. Diagram showing the locations of the ROIs within the scoring plane where the incident primary and scatter energy is scored for validation of the x-ray scatter simulation with a zero-area beam. ROI 5 is located at the center of the scoring plane.

4. Secondary results: When possible, a more complete validation of the x-ray scatter simulation can be achieved by separately scoring the results for:
    a. X-rays that underwent only one Compton event.
    b. X-rays that underwent only one Rayleigh event.
    c. X-rays that underwent more than one scatter event (Compton or Rayleigh).

Statistical Uncertainty

The number of simulated x-rays is such that the statistical uncertainty is 1% or lower on all scored quantities at each VOI (dose) and ROI (scatter).

3.3 Case 3: Mammography and Breast Tomosynthesis

Aim

This case aims to verify the accuracy of x-ray transport and interaction characteristics in mammography and breast tomosynthesis simulations, resulting in the validation of estimates of absorbed dose in the breast glandular tissue and x-ray scatter incident upon the scoring plane. Depending on the application, the dosimetry or the fluence component results may be tested.

Geometry

1. Breast skin is a semi-circular cylinder of thickness (z-direction) 50 mm and radius 100 mm. It is positioned relative to the scoring plane in the center in the y-direction and with the chest wall side congruent with the chest wall edge of the scoring plane. This is the typical mammographic position for a cranio-caudal (CC) view breast. The entrance surface of the breast skin is located 595 mm below the x-ray source at the mammography position (figures 8, 9, and 10).
2. Breast tissue is another semi-circular cylinder, concentric with the breast skin, with thickness (z-direction) 46 mm and radius 98 mm. This results in a skin thickness of 2 mm enveloping the interior breast tissue in all directions except at the chest wall side. The breast tissue is located vertically (z-direction) at the center of the breast skin.
3. The breast compression and breast support plates are rectangular boxes with dimensions in the (x, y, z) directions of 140 mm × 260 mm × 2 mm. The top plate is located immediately above the breast skin in the z-direction (bottom surface touching the top of the breast) and the bottom plate is immediately below the breast skin in the z-direction (top surface touching the bottom of the breast). The centers of both plates are centered with the scoring plane in the (x, y) directions.
4. The scoring plane has sides of 140 mm × 260 mm in the x-y directions and is located 15 mm below the bottom of the breast skin.
5. The body is a rectangular box with dimensions in the (x, y, z) directions of 170 mm × 300 mm × 300 mm, and has its +x surface congruent with the chest wall side of the breast and scoring plane.

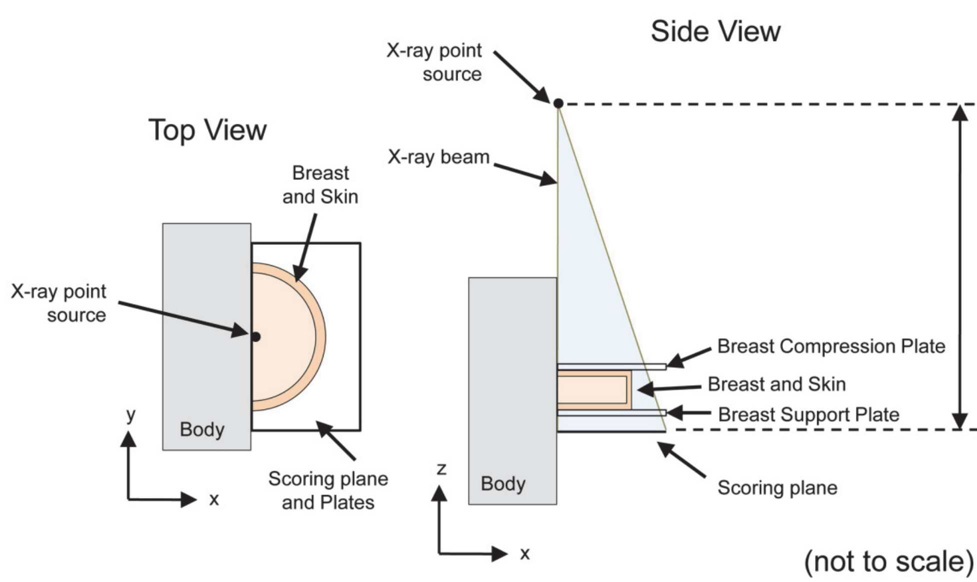

Figure 8. Diagram of the geometry setup for Case #3 with the x-ray source positioned for the mammography acquisition (equivalent to the tomosynthesis 0° angle).

It is centered with the center of the breast in the y- and z- directions. This body volume is present to include any relevant backscatter in the simulations.

Materials

1. The skin of the breast is composed of the material defined as "breast skin."

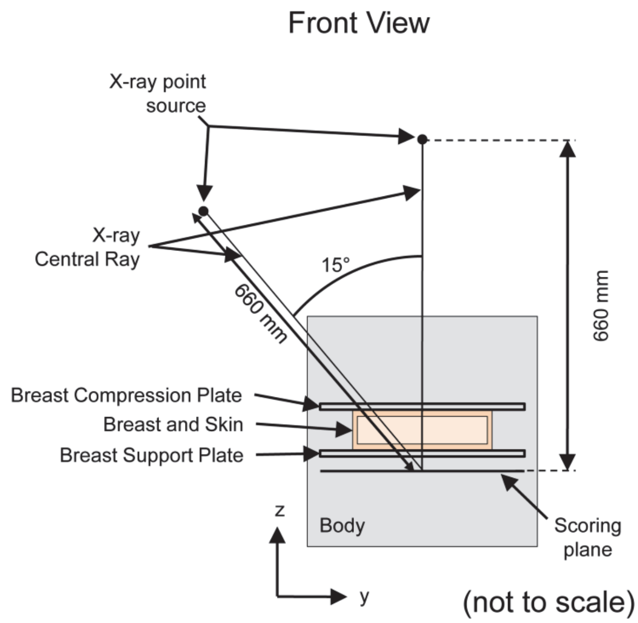

Figure 9. Diagram of the front view of the geometry setup for Case #3 with the x-ray source positioned for both the mammography and the breast tomosynthesis 15° angle acquisitions.

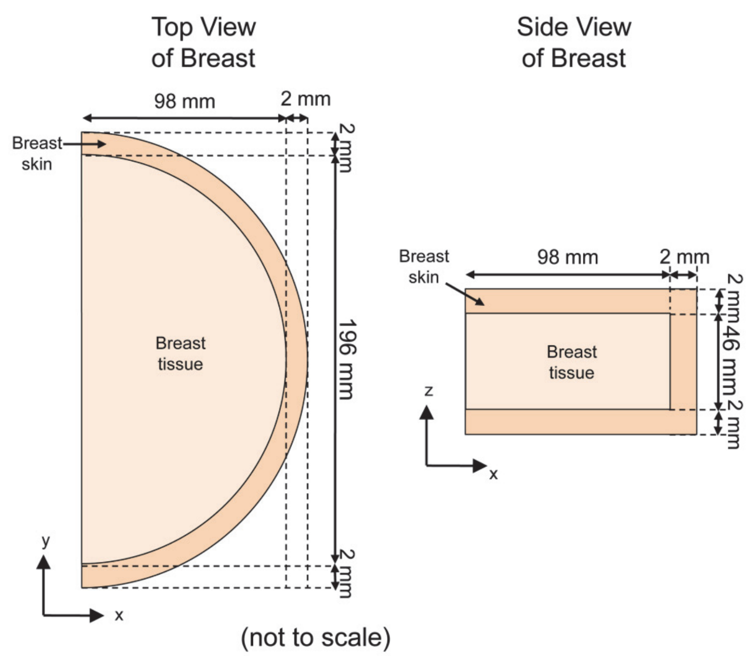

Figure 10. Diagram detailing the dimensions of the simulated breast in Case #3.

2. The interior breast tissue is a homogeneous mixture of 80% breast adipose tissue and 20% breast glandular tissue.
3. The breast compression and support plates are made of PMMA.
4. The body is made of water.
5. The rest of the geometry is filled with air.

Radiation Source

1. Radiation source positions are as follows:
   a. For simulation of mammography and 0° tomosynthesis projection, the source is located at the chest wall edge of the scoring plane in the x-direction, centered with the scoring plane in the y-direction and at z=0.
   b. For simulation of the 15° tomosynthesis projection, the source is rotated 15° about the x-axis, with the center of rotation at the scoring plane.
   c. These positions apply to both the full field and the point spread function simulations.
2. For validation of dosimetry, the x-ray source is an isotropic point source with the x-ray beam collimated for congruence with all four edges of the scoring plane.
3. For validation of x-ray scatter, two types of sources are used as follows:
   a. First test (full-field): Same as point 2 above for validation of dosimetry.
   b. Second test (point-spread function): X-ray point source emits a zero-area beam aimed at the center of the scoring plane.
4. Simulations are performed for the Mo/Mo 30 kVp spectrum and for monoenergetic photons with energy 16.8 keV (equivalent to the mean energy of the spectrum).

Scoring

1. For validation of dosimetry, there are three sets of scoring results:
   a. Total energy deposited in the interior breast tissue, excluding the skin, per initial photon.
   b. Mean glandular dose per initial photon, using the method described in 1999 by Boone[26]:

$$MGD = \frac{\sum_{\text{all hits}} \left\{ g\left(E_{inc}, G\right) \times E_{dep} \right\}}{G \times mass_{\text{breast tissue}}} \tag{3.6}$$

where G is the fraction by weight that is glandular tissue and

$$g\left(E_{inc}, G\right) = \frac{G\left(\frac{\mu_{en}}{\rho}\right)_{gland}}{G\left(\frac{\mu_{en}}{\rho}\right)_{gland} + (1-G)\left(\frac{\mu_{en}}{\rho}\right)_{adip}} \tag{3.7}$$

where

$$\left(\frac{\mu_{en}}{\rho}\right) = \frac{1}{a + b\times E_{inc} + c\times E_{inc}^2 + d\times E_{inc}^3 + e\times E_{inc}^4 + f\times E_{inc}^5} \quad . \tag{3.8}$$

Table 5: Fit coefficient for the mass energy absorption coefficients for breast adipose and glandular tissue

Fit Coefficients	Adipose Tissue	Glandular Tissue
a	4.792×10^{-5}	1.112×10^{-4}
b	-9.042×10^{-5}	-2.324×10^{-4}
c	1.718×10^{-4}	2.594×10^{-4}
d	2.482×10^{-4}	1.296×10^{-4}
e	1.090×10^{-5}	7.977×10^{-6}
f	-1.764×10^{-7}	-1.489×10^{-7}

E_{inc} is the energy, in keV, of the x-ray when the energy deposition occurs, and the fit coefficients *a* through *f* are listed in Table 5. These were obtained by fitting the data provided by NIST[21] using commercial fitting software (TableCurve 2D, Systat Software, San Jose, CA). These fits were performed for x-rays with an energy range of 1.0 keV to 30.0 keV spaced at intervals of 0.5 keV.

c. Energy deposited in 7 cubic volumes of interest (VOIs) inside the breast, each 4,000 mm^3 (20 mm × 20 mm × 10 mm) per initial photon. Five VOIs are located on the central plane parallel to the scoring plane, and two additional VOIs are located directly above and below VOI 3. The locations are shown in Figure 11.

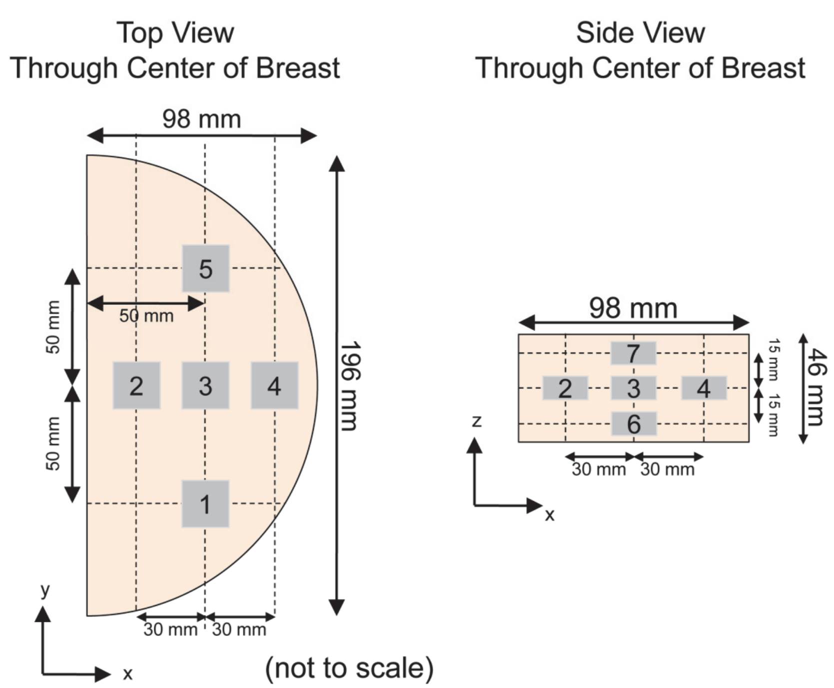

Figure 11. Diagram showing the locations of the VOIs within the simulated breast in Case #3 where the energy deposition is scored for validation of the dosimetry simulation. VOI 3 is located at the center of the breast in the y- and z-directions. VOIs 1, 2, 4, and 5 are at the same z location as VOI 3. VOIs 2, 4, 6, and 7 are at the same y location as VOI 3.

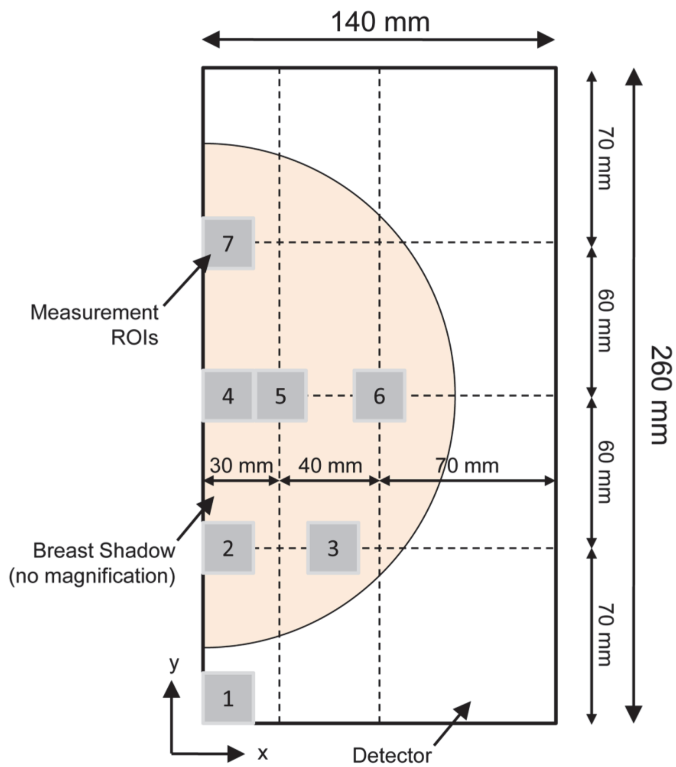

Figure 12. Diagram showing the locations of the ROIs within the scoring plane in Case #3 where the incident primary and scatter energy are scored for validation of the x-ray scatter simulation with a full-field x-ray beam.

2. When validating x-ray primary and scatter components for the first test using a full-field x-ray beam, the scoring is as follows:

   a. Primary x-ray energy per initial photon, incident on 7 regions of interest (ROI), each 20 mm × 20 mm, throughout the scoring plane, according to Figure 12.

   b. Scatter x-ray energy per initial photon, incident on the same 7 ROIs.

   These ROIs correspond to 20 mm × 20 mm regions with the following image indices:

   1: (0, 0)

   2: (0, 3)

   3: (2, 3)

   4: (0, 6)

   5: (1, 6)

   6: (3, 6)

   7: (0, 9)

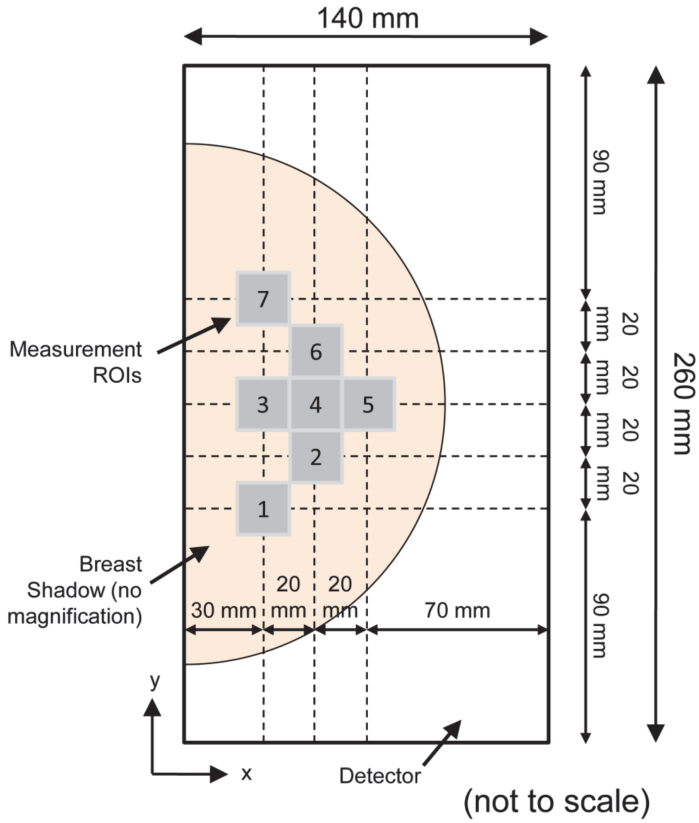

Figure 13. Diagram showing the locations of the ROIs within the scoring plane in Case #3 where the incident primary and scatter energy are scored for validation of the x-ray scatter simulation with a zero-area beam. ROI 5 is located at the center of the scoring plane.

3. When validating x-ray primary and scatter results for the second test using a zero-area beam resulting in a point-spread function, the scoring should be as follows:

   a. Scatter x-ray energy per initial photon, incident on 7 ROIs, each 20 mm × 20 mm, throughout the scoring plane, according to Figure 13.

   b. Primary x-ray energy per initial photon, incident on ROI 5, according to Figure 13.

   These ROIs correspond to 20 mm × 20 mm regions with the following image indices:

   1: (1, 4)

   2: (2, 5)

   3: (1, 6)

   4: (2, 6)

   5: (3, 6)

   6: (2, 7)

   7: (1, 8)

4. Secondary results: When possible, a more complete validation of the x-ray primary and scatter simulation can be achieved by discriminating the results by:
    a. X-rays that underwent only one Compton event.
    b. X-rays that underwent only one Rayleigh event.
    c. X-rays that underwent more than one scatter event (Compton or Rayleigh).

Statistical Uncertainty

The number of simulated x-rays is such that the statistical uncertainty is 1% or lower on all scored quantities.

3.4 Case 4: Computed Tomography with Simple Solids

Aim

This case aims to verify the accuracy of x-ray transport and interaction characteristics in computed tomography in addition to x-ray source rotation, resulting in the validation of estimates of absorbed dose in a simple CT phantom.

Geometry

Body phantom is a cylinder of height (z-direction) 3,000 mm (to approximate an infinite cylinder) and radius 160 mm (Figure 14). The center of the cylinder is placed at the x-ray source isocenter of rotation, which is the origin (x=y=z=0).

Materials

1. The body phantom is made of PMMA.
2. The rest of the geometry is filled with air.

Radiation Source

1. The source is an isotropic x-ray point source collimated to a fan beam with dimensions, measured at the center of the body phantom, of width (y-direction) equal to the body diameter (320 mm) and thickness (z-direction) of t. The values for t are provided in Table 6.
2. The rotation radius of the x-ray source about the isocenter, located at the center of the body phantom, is 600 mm.
3. For the first test with the scoring of dose in four contiguous cylindrical segments, the x-ray source is located at the 0° position (at coordinates x = –600 mm and y = z = 0), as shown in Figure 14.

Table 6: Simulation parameters for Case #4

Parameter	Number	Minimum	Maximum	Increment
Fan beam thickness, t (mm)	2	10	80	70
Projection Angles (deg)				
First Test	1	0	0	–
Second Test – Discrete	36	0	350	10
Second Test – Random	∞	0	360	–

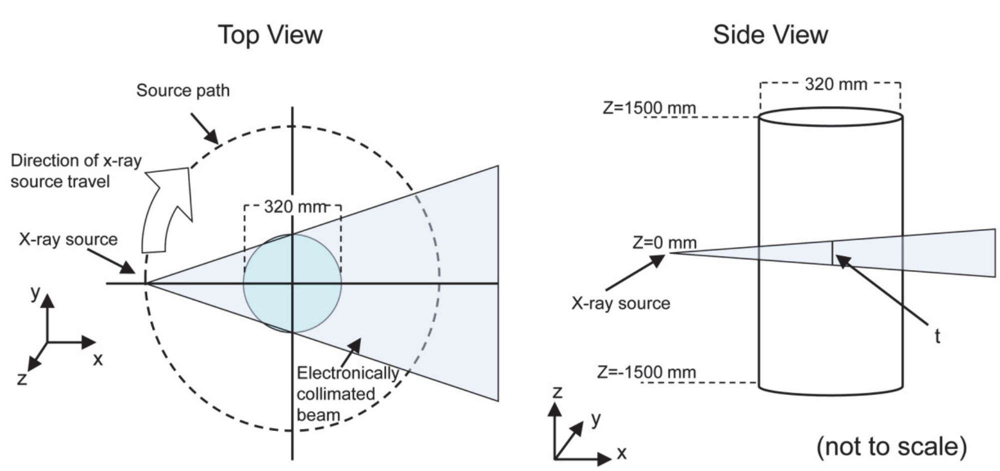

Figure 14. Diagram of the geometry setup for Case #4.

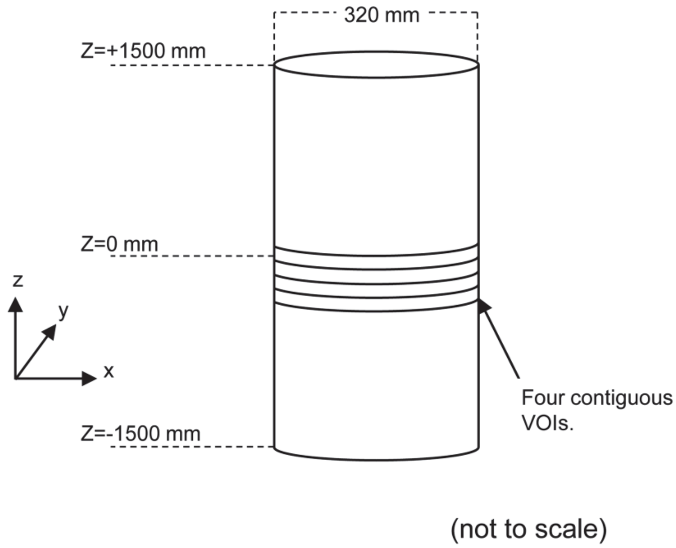

Figure 15. Diagram showing the locations of the four cylindrical VOIs within the simulated body phantom in Case #4 where the energy deposition is scored for the first test of this CT dosimetry simulation. This simulation is only performed with the x-ray source at the 0° position.

4. For the second test with the scoring of dose in two 10 mm diameter cylinders, two different source types are simulated:
   a. Source rotated 360° about the isocenter in 10° increments, with 36 evenly spaced simulations performed.
   b. Angular position of source is randomly sampled for each x-ray emitted from the continuous distribution of 360° about the isocenter.
5. Simulations are performed for the W/Al 120 kVp spectrum and for monoenergetic photons with energy 56.4 keV (equivalent to the mean energy of the spectrum).

Scoring

1. For the first test, the scoring is the energy deposited in four contiguous cylindrical segments from a single projection, as shown in Figure 15. Each cylindrical segment is an axial tomographic section of the phantom with thickness 10 mm, with centers located at z = 0 mm, z = 10 mm, z = 20 mm, and z = 30 mm (either in the positive or negative z direction).

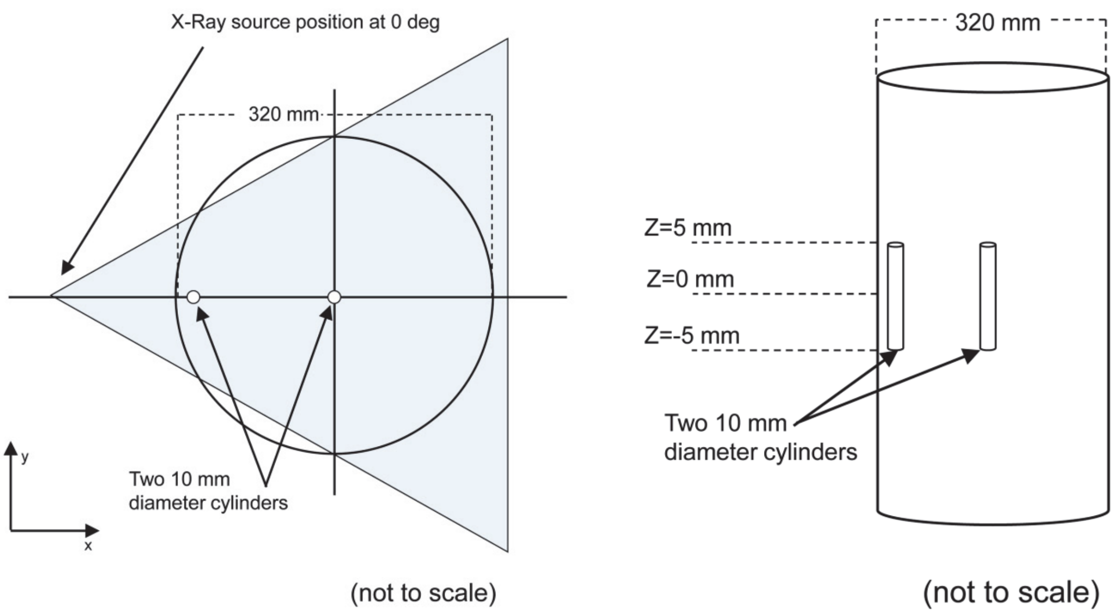

Figure 16. Diagram showing the locations of the two cylindrical VOIs within the simulated body phantom in Case #4 where the energy deposition is scored for the second test of this CT dosimetry simulation. One set of simulations is performed with the x-ray source positioned at 36 discrete projection angles, and another simulation is performed with the x-ray source positioned at randomly sampled projection angles about the 360°.

2. For the second test, the scoring is the energy deposited in two 10 mm diameter PMMA cylinders with height (z-direction) of 100 mm from −50 mm to +50 mm, as shown in Figure 16. One cylinder is located at the center of the body phantom and one is located with its center 150 mm from the center of the body phantom.

Statistical Uncertainty

The number of simulated x-rays is such that the statistical uncertainty is 1% or lower on all scored quantities at each VOI.

3.5 Case 5: Computed Tomography with a Voxelized Solid

Aim

This case aims to verify the accuracy of voxel-based x-ray transport and interaction characteristics in computed tomography, in addition to x-ray source rotation, resulting in the validation of estimates of absorbed dose in a complex, voxelized CT phantom.

Even though this simulation uses a relatively thin fan beam, this case may also be useful for verification of dosimetry simulations involving voxelized solids in other modalities, such as radiography and body tomosynthesis. For these, comparison of the results for a single or a limited number of projection angles may be sufficient.

Geometry

Geometry is exactly the same as that defined for Case #4, but with a voxelized box replacing the cylindrical body phantom (Figure 17). The box has dimensions of thickness (x-direction) 320 mm, width

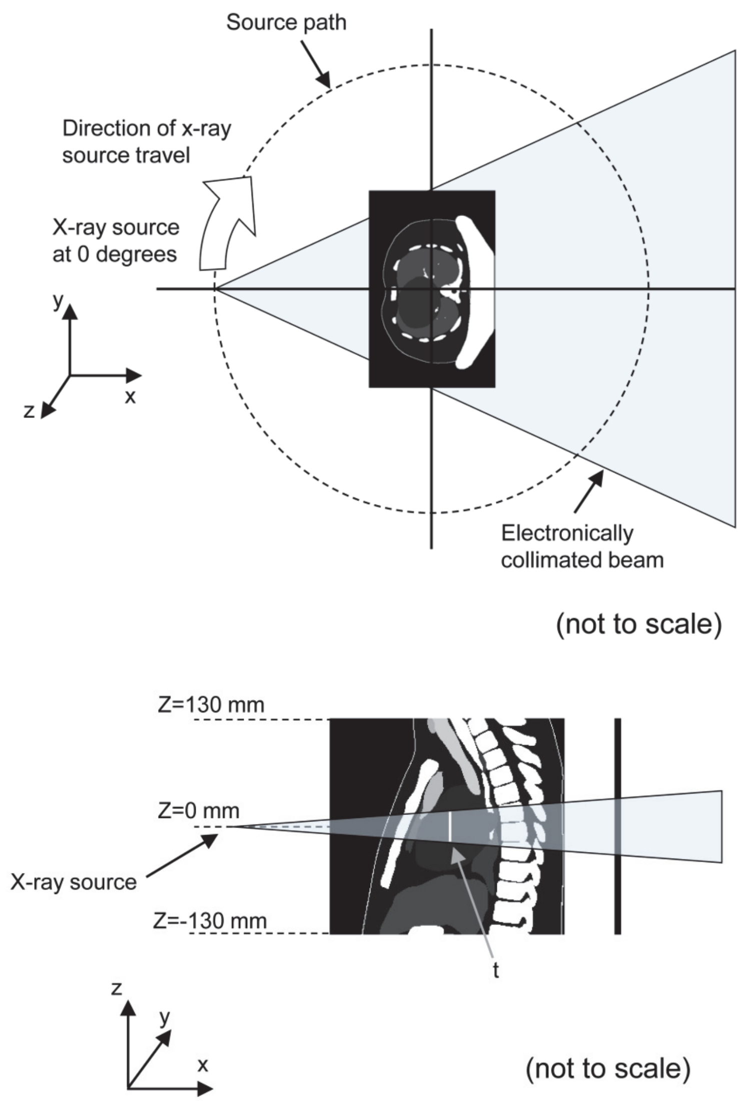

Figure 17. Diagram of the geometry setup for Case #5.

Table 7: Simulation parameters for Case #5

Projection Angles (deg)	Number	Minimum	Maximum	Increment
Discrete	8	0	345	45
Random	∞	0	360	–

(y-direction) 500 mm, and height (z-direction) 260 mm, containing 320 × 500 × 260 voxels. This voxelized volume contains the description of the torso portion of a human patient. Each voxel is 1.0 mm × 1.0 mm × 1.0 mm.

Materials

1. The three-dimensional (3D) image with the information for the material content of the voxelized volume is available for download in the electronic resources included with this report. This reference case is the XCAT model, courtesy of Ehsan Samei and Paul Segars of Duke University, to serve as a reference platform for Monte Carlo simulations. Care should be taken to use this volume with the correct orientation in the Monte Carlo simulation. The voxels in the image contain values ranging from 0 to 19 that correspond to material definitions also available for download in the electronic resources included with this report.
2. The rest of the geometry is filled with air.

Radiation Source

1. The isotropic x-ray point source is collimated to a fan beam with dimensions, measured at the center of the voxelized volume, of width (y-direction) equal to the voxelized volume (500 mm) and thickness (z-direction) of 10 mm.
2. The rotation radius of the x-ray source about the isocenter, located at the center of the body phantom, is 600 mm.
3. The 0° position of the x-ray source is located at coordinates x = –600 mm and y = z = 0, as shown in Figure 17, and increasing angle projections are in the direction marked in the same figure.
4. Two different source types are simulated (see Table 7):
    a. Source rotated 360° about the isocenter in 45° increments, with 8 evenly spaced simulations performed.
    b. Angular position of the source is randomly sampled for each x-ray emitted from the continuous distribution of 360° about the isocenter.
5. Simulations are performed for the W/Al 120 kVp spectrum and for monoenergetic photons with energy 56.4 keV (equivalent to the mean energy of the spectrum).

Scoring

The scoring is the energy deposited in all the voxels with values 3 to 19, separated by organ/material.

Statistical Uncertainty

The number of simulated x rays is such that the statistical uncertainty is 1% or lower on dose scored in all organ/materials except for the adrenals (voxel value = 12).

3.6 Case 6: X-ray Production

Aim

This case aims to verify the accuracy of electron transport and x-ray generation in typical tube targets in mammography and radiography. The results will depend on the physical models used to simulate Bremsstrahlung emission and inner shell ionizations, as well as the internal tables on characteristic x-ray emission energies.

Geometry

1. Target is a slab of height 25 mm, width 80 mm, and thickness 10 mm. The center of the front face of the slab is at the geometry origin (x=0, y=0, z=0). The slab is tilted at an angle θ relative to the +z axis (Figure 18).
2. Simulations are performed for two target materials and their corresponding target angles and incident electron energies, as given in Table 8.

Materials

1. Target material is either molybdenum or tungsten, depending on the incident electron kinetic energy.
2. The rest of the geometry is filled with a vacuum.

Table 8: Simulation parameters for Case #6

Modality	Target Material	Incident Electron Kinetic Energy (keV)	Anode Angle (deg)
Mammography	Mo	30	15
Radiography	W	100	11

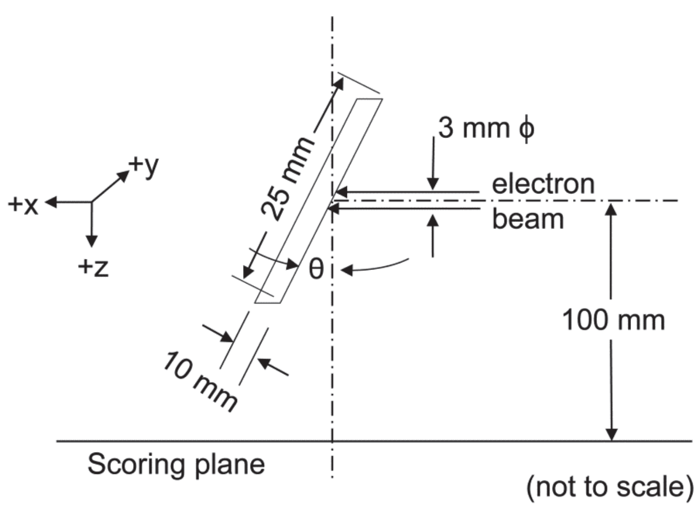

Figure 18. Diagram of the geometry setup for Case #6.

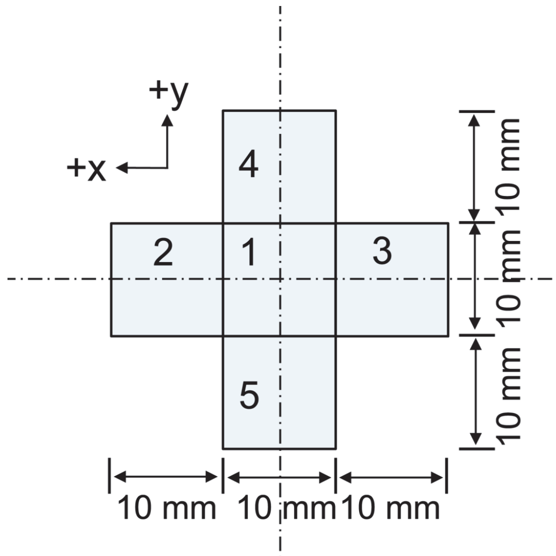

Figure 19. Diagram of the scoring areas for Case #6.

Radiation Source

1. Radiation source is an electron beam parallel to the +x direction that uniformly covers a circle of diameter 3 mm centered at the geometry origin (x=0, y=0, z=0).
2. Simulations are performed for monoenergetic electrons with energies given in Table 8.

Scoring

1. Energy distribution is scored in 1 keV bins for photons crossing the plane z = +100 mm at five square areas, 10 mm × 10 mm each. The locations of the scoring areas are given in Figure 19.
2. For each square area, the output is the energy distribution and the integral planar energy fluence. Areas 2, 1, and 3 reflect the heel effect, while areas 4, 1, and 5 reflect symmetry.

Statistical Uncertainty

The number of simulated source particles is such that the statistical uncertainty is 1% on each bin of the scored x-ray energy distribution from 7.5 keV and up.

4. Results

Detailed tabular results for all six cases simulated with the Monte Carlo packages listed in Table 2 are available for download in the electronic resources included with this report. To aid in the comparison of the results between the different Monte Carlo packages included in this report, some tables and graphs are included here for some specific simulation conditions that are representative of all the results. Additional graphs are included in the results spreadsheets available for download in the electronic resources. All uncertainties shown in tables and graphs are due only to the statistical uncertainties from the Monte Carlo simulations and do not include any uncertainties or limitations of the underlying physics models.

It should be noted that the ranges of results presented in this report are those found from the Monte Carlo simulations performed as a part of this task group effort. They represent the best attempts of the task group members. However, they do not necessarily reflect the best possible performance or accuracy of each Monte Carlo package. As such, to consider a new simulation validated, the results obtained do not necessarily have to be within the ranges presented here. It is up to the investigator's discretion as to when his/her results should be considered consistent with those found by this task group, and therefore whether his/her code can be considered validated.

The comparison of simulated results with experimental measurements is still an essential step in the process of validating a new simulation algorithm. However, the possibility of comparing simulation results among different codes using clearly defined geometries, material composition, and scoring methods eliminates many of the sources of variability and error found in experimental measurements, and it provides an insight into the inner workings of the simulation code at a precision level beyond the accuracy of standard experimental measurements.

All results spreadsheets that are available for download in the electronic resources included with this report include timing information for the simulations implemented with the four Monte Carlo packages listed in Table 2. The timing information for each simulation is presented in two forms: (i) the mean time per history simulated, and (ii) the total simulation time needed to achieve an uncertainty of 1% for a specific scored quantity. Given the possible use of different variance reduction techniques, the latter quantity in general provides more complete information regarding simulation times than the former. The timing results are estimated assuming a sequential execution of the simulation on a single core of a modern CPU. The simulations can be run serially or in parallel on a cluster of computers and, therefore, the effective simulation time depends on the amount of computational resources invested in the execution. Each scored quantity for which the timing to achieve 1% uncertainty is provided is specified by a color highlight in the appropriate cell in the spreadsheet.

4.1 Case 1: Half Value Layer

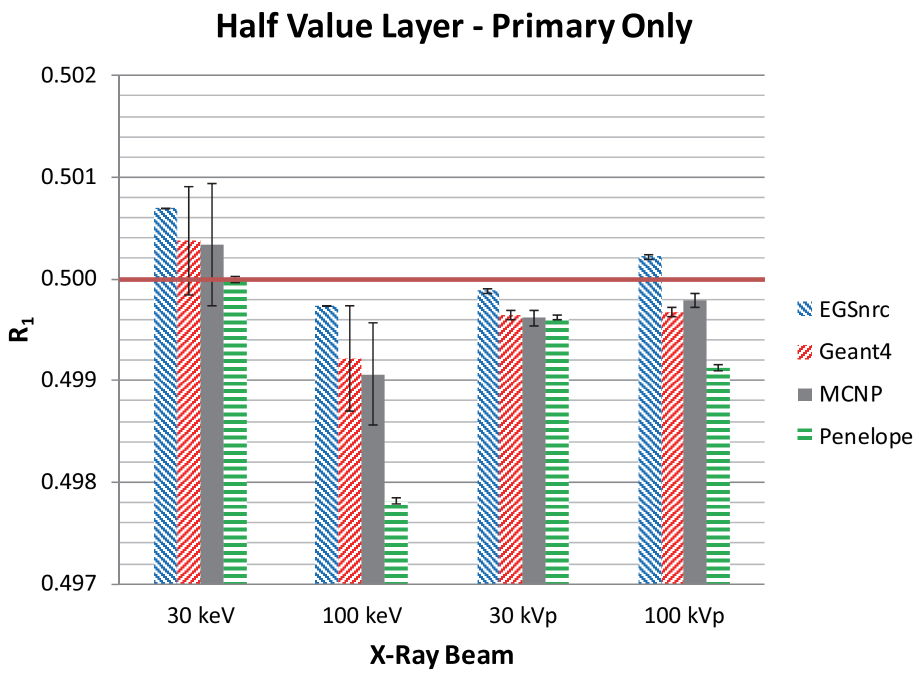

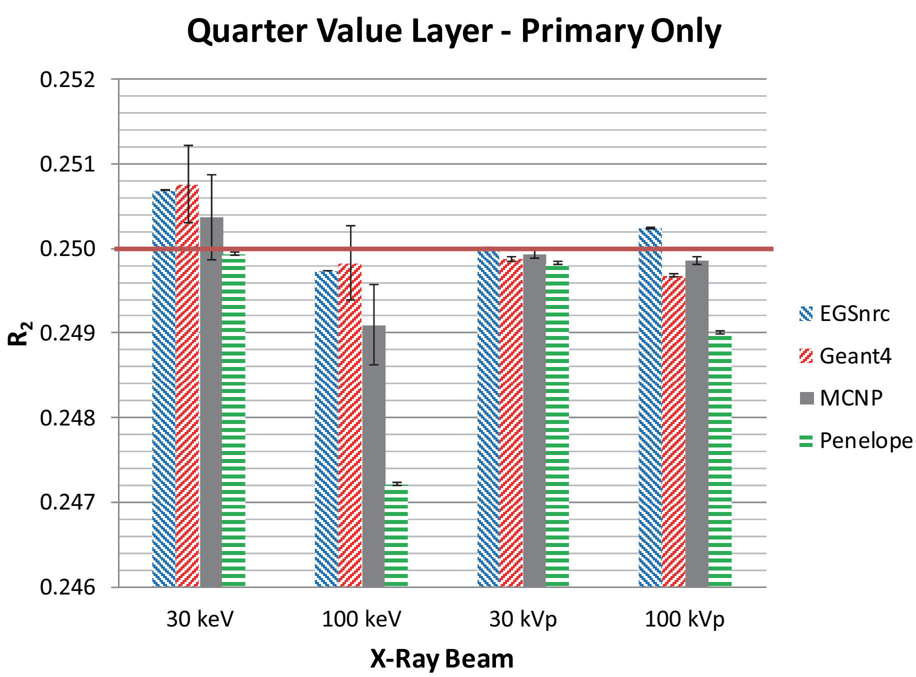

Figure 20. Calculated values of the HVL (top) and QVL (bottom) based on just primary photons in Case #1 for the four Monte Carlo packages included in Table 2. Note the narrow range of the vertical scale and the presence of the uncertainty bars due to the statistical uncertainty in each simulation.

4.2 Case 2: Radiography and Body Tomosynthesis

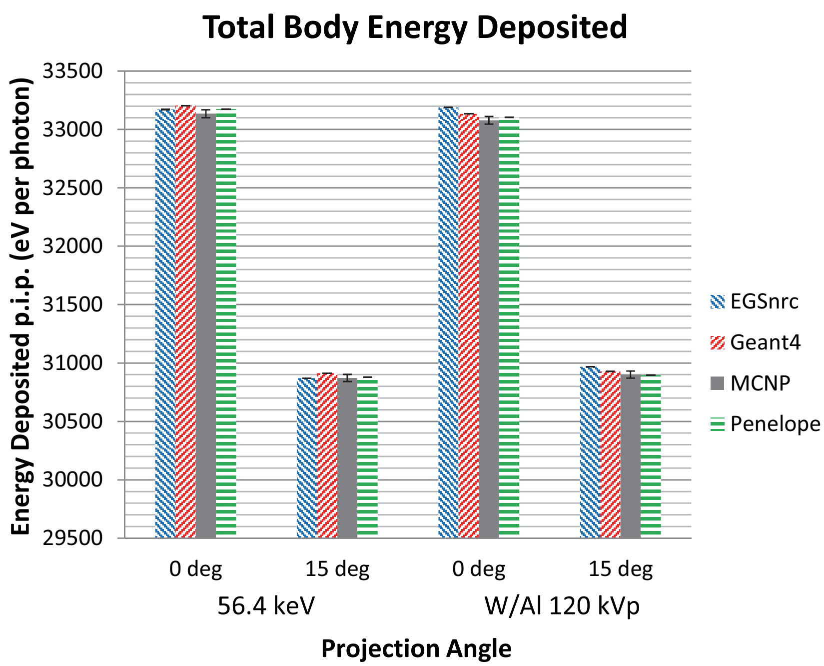

Figure 21. Energy deposition in the whole body per initial photon in Case #2 for the four Monte Carlo packages included in Table 2. Note the narrow range of the vertical scale and the presence of the uncertainty bars due to the statistical uncertainty in each simulation.

Table 9: Minimum and maximum ratios to the mean values for the energy deposited in the entire body volume for all Monte Carlo simulations performed for Case #2 with the full-field x-ray beam. Statistical uncertainties are 0.00014% to 0.10%.

	Radiography (0 deg)	Tomosynthesis (15 deg)
56.4 keV	0.999 – 1.001	1.000 – 1.001
W/Al 120 kVp	0.999 – 1.002	0.999 – 1.001

Table 10: Minimum and maximum ratios to the mean values for the energy deposited in each VOI on the body volume for all Monte Carlo simulations performed for Case #2 with the full-field x-ray beam. Statistical uncertainties are 0.004% to 0.26%.

	56.4 keV		W/Al 120 kVp	
Body VOI	Radiography (0 deg)	Tomosynthesis (15 deg)	Radiography (0 deg)	Tomosynthesis (15 deg)
1	0.999 – 1.003	0.998 – 1.002	0.997 – 1.002	0.997 – 1.003
2	0.998 – 1.003	0.999 – 1.003	0.997 – 1.003	0.997 – 1.002
3	0.994 – 1.003	0.996 – 1.003	0.990 – 1.007	0.990 – 1.006
4	0.999 – 1.003	0.998 – 1.002	0.997 – 1.003	0.997 – 1.002
5	0.998 – 1.003	0.997 – 1.004	0.997 – 1.002	0.995 – 1.007
6	0.994 – 1.011	0.996 – 1.010	0.995 – 1.012	0.996 – 1.011
7	0.986 – 1.005	0.986 – 1.005	0.982 – 1.010	0.982 – 1.009
8	0.999 – 1.002	0.999 – 1.003	0.996 – 1.005	0.995 – 1.005
9	0.992 – 1.014	0.992 – 1.016	0.992 – 1.020	0.989 – 1.022

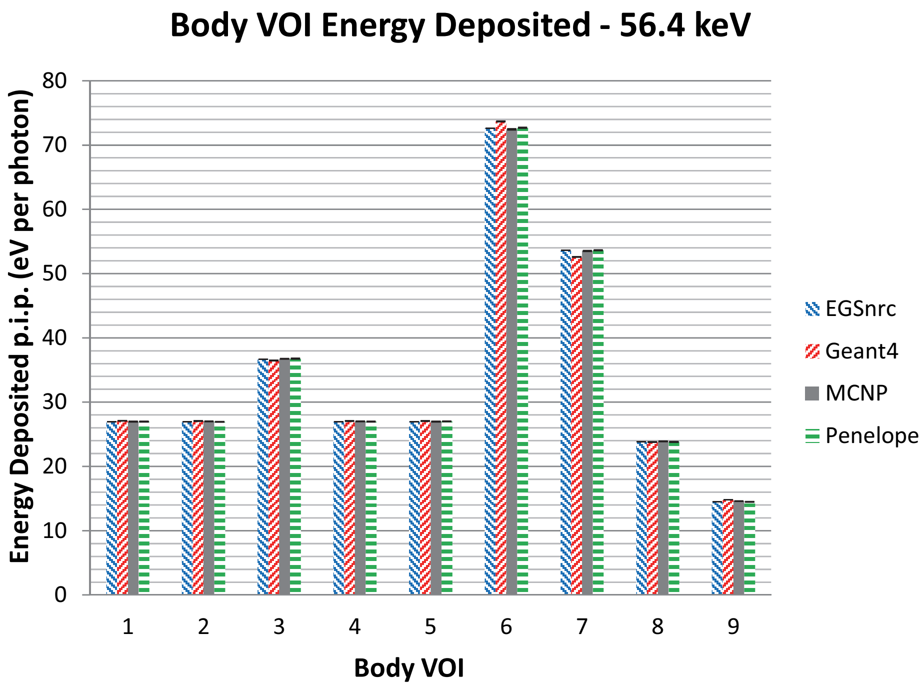

Figure 22. Energy deposition in the VOIs in the body per initial photon for the radiography (0° projection) for the 56.4 keV x-ray energy simulations of Case #2 with the four Monte Carlo packages included in Table 2.

Table 11: Minimum and maximum ratios to the mean values for the primary energy incident in each ROI at the scoring plane for all Monte Carlo simulations performed for Case #2 with the full field x-ray beam. Statistical uncertainties are 0.004% to 0.61%.

	56.4 keV		W/Al 120 kVp	
Scoring Plane ROI	**Radiography (0 deg)**	**Tomosynthesis (15 deg)**	**Radiography (0 deg)**	**Tomosynthesis (15 deg)**
1	0.988 – 1.012	0.999 – 1.001	0.984 – 1.010	0.997 – 1.003
2	0.986 – 1.012	0.998 – 1.002	0.986 – 1.007	0.997 – 1.003
3	0.984 – 1.017	0.988 – 1.014	0.982 – 1.008	0.984 – 1.009
4	0.980 – 1.015	0.987 – 1.014	0.982 – 1.014	0.983 – 1.016
5	0.982 – 1.017	0.985 – 1.015	0.984 – 1.010	0.988 – 1.008
6	0.980 – 1.015	0.987 – 1.014	0.988 – 1.006	0.986 – 1.009
7	0.984 – 1.015	0.986 – 1.015	0.985 – 1.010	0.989 – 1.008

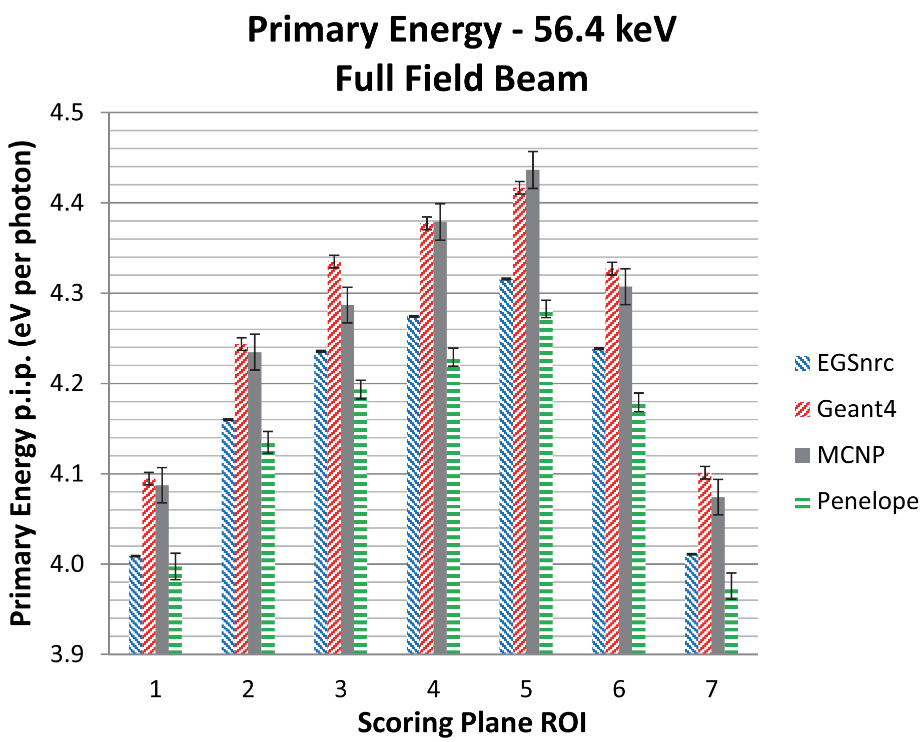

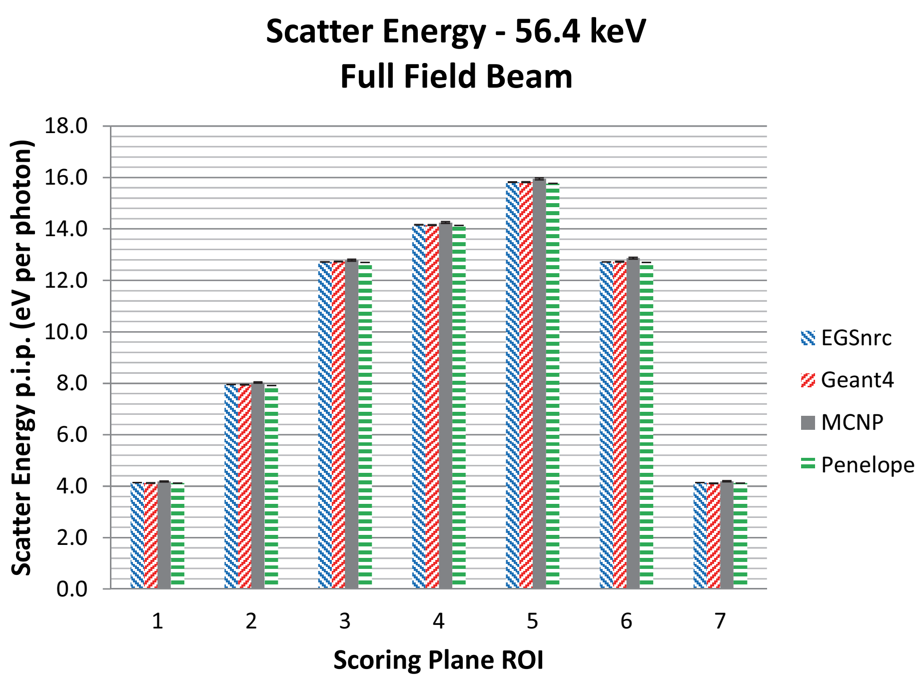

Figure 23. Primary component (top) and scatter component (bottom) of energy incident on the scoring plane ROIs per initial photon with the full field x-ray beam for the radiography (0° projection) 56.4 keV x-ray energy simulations of Case #2 with the four Monte Carlo packages included in Table 2.

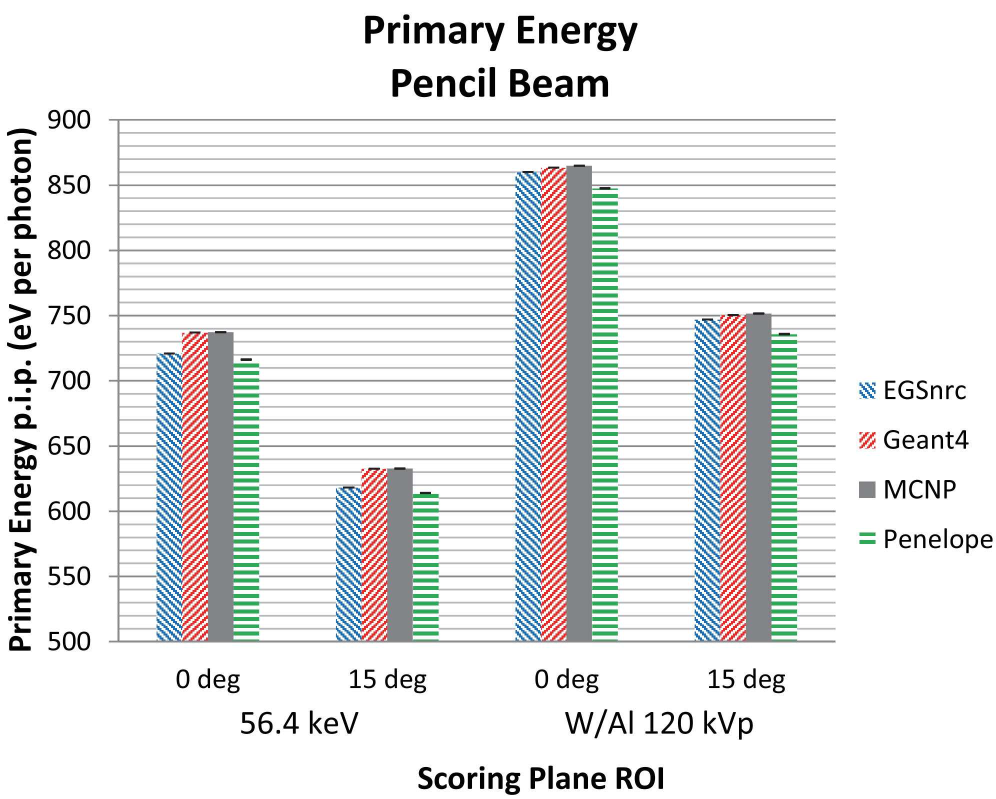

Figure 24. Primary component (both 0° and 15° projections) of photon energy incident on the scoring plane ROI 5 per initial photon with the zero-area beam for both x-ray beams of Case #2 with the four Monte Carlo packages included in Table 2.

Table 12: Minimum and maximum ratios to the mean values for the scatter energy incident in each ROI at the scoring plane for all Monte Carlo simulations performed for Case #2 with the full field x-ray beam. Statistical uncertainties are 0.01% to 0.60%.

	56.4 keV		W/Al 120 kVp	
Scoring Plane ROI	**Radiography (0 deg)**	**Tomosynthesis (15 deg)**	**Radiography (0 deg)**	**Tomosynthesis (15 deg)**
1	0.995 – 1.010	0.994 – 1.004	0.993 – 1.008	0.993 – 1.006
2	0.995 – 1.008	0.995 – 1.004	0.995 – 1.006	0.995 – 1.007
3	0.997 – 1.004	0.995 – 1.004	0.995 – 1.007	0.994 – 1.007
4	0.998 – 1.005	0.994 – 1.009	0.995 – 1.007	0.994 – 1.006
5	0.996 – 1.007	0.996 – 1.008	0.994 – 1.007	0.994 – 1.008
6	0.995 – 1.009	0.995 – 1.010	0.994 – 1.006	0.993 – 1.006
7	0.993 – 1.012	0.993 – 1.012	0.992 – 1.008	0.993 – 1.012

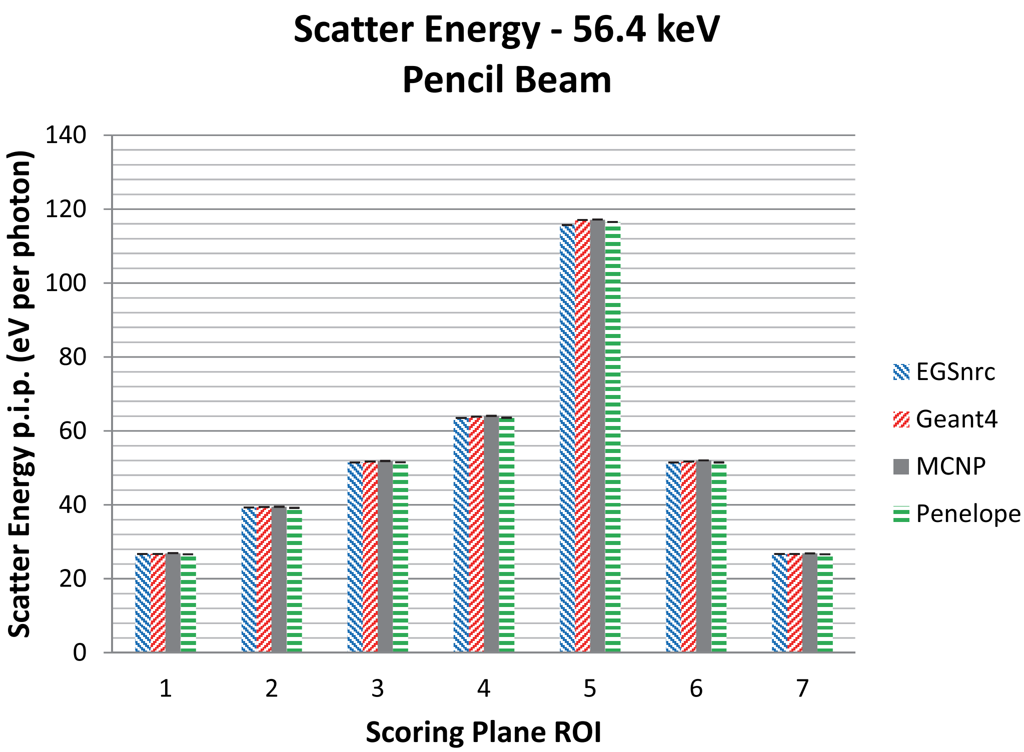

Figure 25. Scatter component of photon energy incident on the scoring plane ROIs per initial photon for the 0° projection and 56.4 keV x-ray energy with the zero-area beam of Case #2 for the four Monte Carlo packages included in Table 2.

Table 13: Minimum and maximum ratios to the mean values for the primary energy incident in ROI 5 at the scoring plane for all Monte Carlo simulations performed for Case #2 with the zero-area x-ray beam. Statistical uncertainties are 0.002% to 0.04%.

	Radiography (0 deg)	Tomosynthesis (15 deg)
56.4 keV	0.984 – 1.013	0.983 – 1.013
W/Al 120 kVp	0.987 – 1.007	0.986 – 1.007

Table 14: Minimum and maximum ratios to the mean values for the scatter energy incident in each ROI at the scoring plane for all Monte Carlo simulations performed for Case #2 with the zero-area x-ray beam. Statistical uncertainties are 0.004% to 0.25%.

	56.4 keV		W/Al 120 kVp	
Scoring Plane ROI	Radiography (0 deg)	Tomosynthesis (15 deg)	Radiography (0 deg)	Tomosynthesis (15 deg)
1	0.996 – 1.007	0.995 – 1.007	0.996 – 1.007	0.996 – 1.008
2	0.997 – 1.004	0.998 – 1.004	0.996 – 1.008	0.997 – 1.007
3	0.997 – 1.004	0.997 – 1.005	0.995 – 1.006	0.996 – 1.005
4	0.996 – 1.005	0.996 – 1.004	0.997 – 1.005	0.996 – 1.005
5	0.992 – 1.005	0.993 – 1.005	0.999 – 1.001	0.998 – 1.001
6	0.996 – 1.007	0.996 – 1.006	0.996 – 1.006	0.995 – 1.006
7	0.996 – 1.006	0.995 – 1.007	0.997 – 1.008	0.994 – 1.007

4.3 Case 3: Mammography and Breast Tomosynthesis

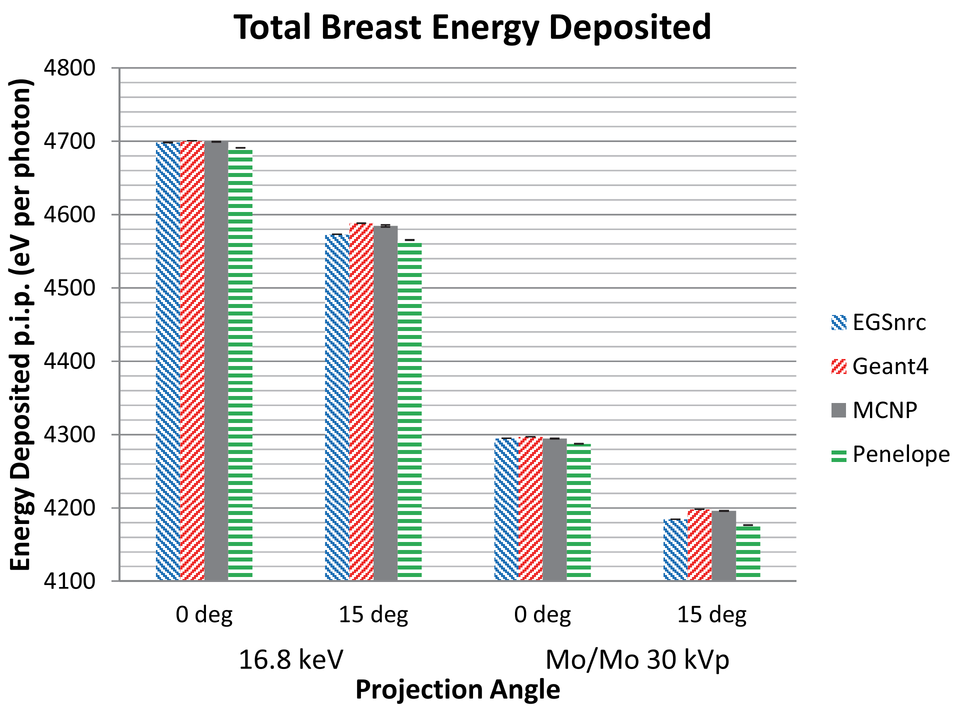

Figure 26. Energy deposition in the breast tissue of Case #3 for the four Monte Carlo packages in Table 2.

Table 15: Minimum and maximum ratios to the mean values for the energy deposited in the entire breast volume for all Monte Carlo simulations performed for Case #3 with the full-field x-ray beam. Statistical uncertainties are 0.0016% to 0.03%.

	Mammography (0 deg)	Tomosynthesis (15 deg)
16.8 keV	0.999 – 1.001	0.997 – 1.002
Mo/Mo 30 kVp	0.999 – 1.001	0.997 – 1.002

Table 16: Minimum and maximum ratios to the mean values for the glandular dose in the entire breast volume for all Monte Carlo simulations performed for Case #3 with the full-field x-ray beam. Statistical uncertainties are 0.0016% to 0.03%.

	Mammography (0 deg)	Tomosynthesis (15 deg)
16.8 keV	0.999 – 1.002	0.997 – 1.004
Mo/Mo 30 kVp	0.997 – 1.003	0.998 – 1.003

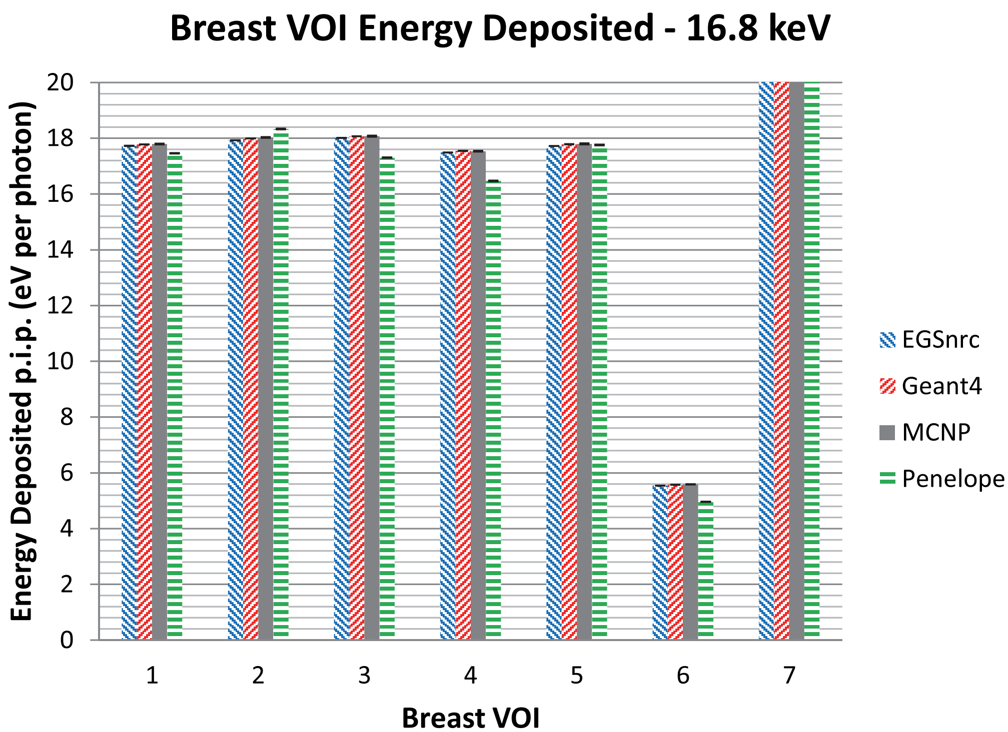

Figure 27. Energy deposition per initial photon in the VOIs in the breast for the mammography (0° projection) for the 16.8 keV x-ray energy simulations of Case #3 with the four Monte Carlo packages included in Table 2. Note that the columns for VOI 7 extend beyond the y-axis scale (to about 56 eV per photon), to enhance visibility of the results of the other VOIs.

Table 17: Minimum and maximum ratios to the mean values for the energy deposited on each VOI in the breast volume for all Monte Carlo simulations performed for Case #3 with the full-field x-ray beam. Statistical uncertainties are 0.02% to 1.03%.

	16.8 keV		Mo/Mo 30 kVp	
Breast VOI	**Mammography (0 deg)**	**Tomosynthesis (15 deg)**	**Mammography (0 deg)**	**Tomosynthesis (15 deg)**
1	0.987 – 1.006	0.983 – 1.009	0.998 – 1.002	0.997 – 1.003
2	0.992 – 1.014	0.984 – 1.009	0.999 – 1.002	0.998 – 1.003
3	0.968 – 1.012	0.983 – 1.008	0.998 – 1.001	0.998 – 1.002
4	0.954 – 1.017	0.983 – 1.008	0.999 – 1.001	0.997 – 1.003
5	0.998 – 1.002	0.982 – 1.012	0.997 – 1.002	0.997 – 1.003
6	0.917 – 1.031	0.985 – 1.009	0.997 – 1.002	0.996 – 1.005
7	0.986 – 1.005	0.980 – 1.009	0.999 – 1.001	0.997 – 1.003

Table 18: Minimum and maximum ratios to the mean values for the primary photon energy incident on each ROI at the scoring plane for all Monte Carlo simulations performed for Case #3 with the full field x-ray beam. Statistical uncertainties are 0.03% to 2.29%.

	16.8 keV		Mo/Mo 30 kVp	
Scoring Plane ROI	**Mammography (0 deg)**	**Tomosynthesis (15 deg)**	**Mammography (0 deg)**	**Tomosynthesis (15 deg)**
1	0.999 – 1.001	0.996 – 1.004	0.999 – 1.001	0.996 – 1.004
2	0.993 – 1.007	0.982 – 1.038	0.992 – 1.007	0.989 – 1.009
3	0.990 – 1.008	0.988 – 1.017	0.992 – 1.009	0.990 – 1.010
4	0.993 – 1.004	0.992 – 1.009	0.990 – 1.009	0.991 – 1.012
5	0.990 – 1.011	0.993 – 1.006	0.993 – 1.008	0.989 – 1.017
6	0.991 – 1.010	0.992 – 1.004	0.995 – 1.006	0.990 – 1.010
7	0.992 – 1.007	0.991 – 1.009	0.991 – 1.009	0.990 – 1.010

Table 19: Minimum and maximum ratios to the mean values for the energy of scattered photons incident on each ROI at the scoring plane for all Monte Carlo simulations performed for Case #3 with the full-field x-ray beam. Statistical uncertainties are 0.02% to 3.11%.

	16.8 keV		Mo/Mo 30 kVp	
Scoring Plane ROI	**Mammography (0 deg)**	**Tomosynthesis (15 deg)**	**Mammography (0 deg)**	**Tomosynthesis (15 deg)**
1	0.992 – 1.004	0.995 – 1.007	0.989 – 1.010	0.989 – 1.014
2	0.974 – 1.029	0.986 – 1.018	0.981 – 1.022	0.981 – 1.026
3	0.976 – 1.019	0.984 – 1.016	0.984 – 1.015	0.987 – 1.016
4	0.978 – 1.030	0.982 – 1.016	0.980 – 1.027	0.983 – 1.026
5	0.977 – 1.019	0.990 – 1.020	0.985 – 1.014	0.985 – 1.017
6	0.977 – 1.025	0.966 – 1.054	0.987 – 1.010	0.987 – 1.019
7	0.970 – 1.020	0.973 – 1.028	0.980 – 1.021	0.980 – 1.020

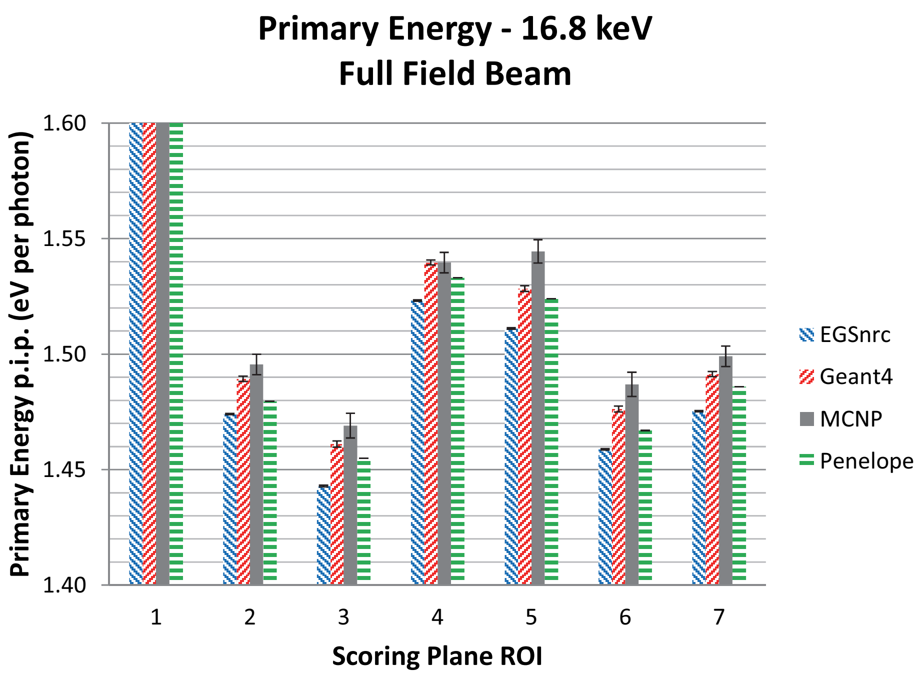

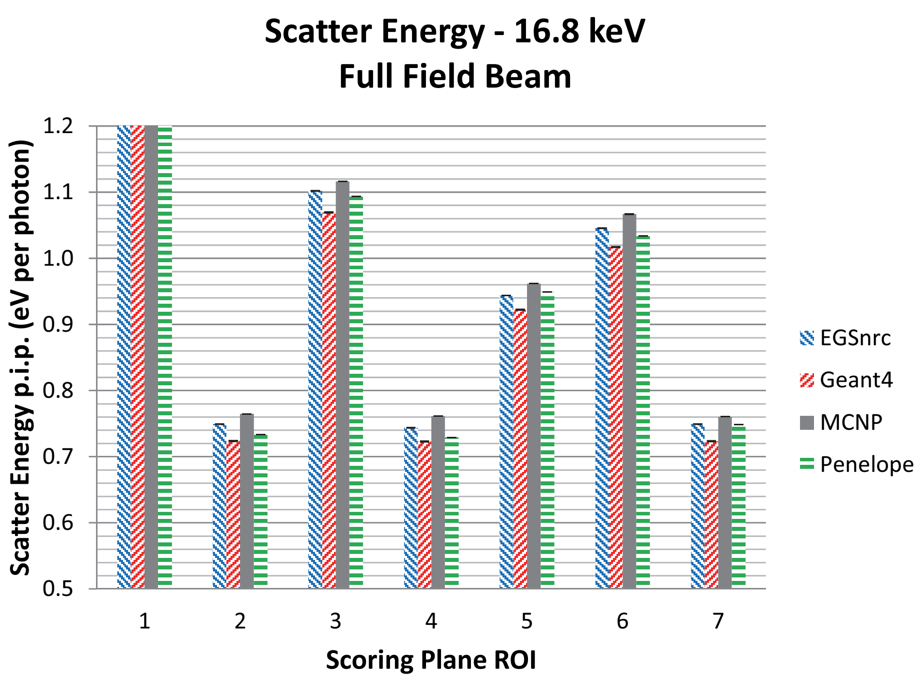

Figure 28. Primary component (top) and scattered component (bottom) of photon energy incident per initial photon on the scoring plane ROIs with the full-field x-ray beam for the mammography (0° projection) 16.8 keV x-ray energy simulations of Case #3 with the four Monte Carlo packages included in Table 2. Note that the columns for ROI 1 for both graphs extend beyond the y-axis scale (to about 110 eV per initial photon and 3.4 eV per initial photon, respectively), to enhance visibility of the results of the other ROIs.

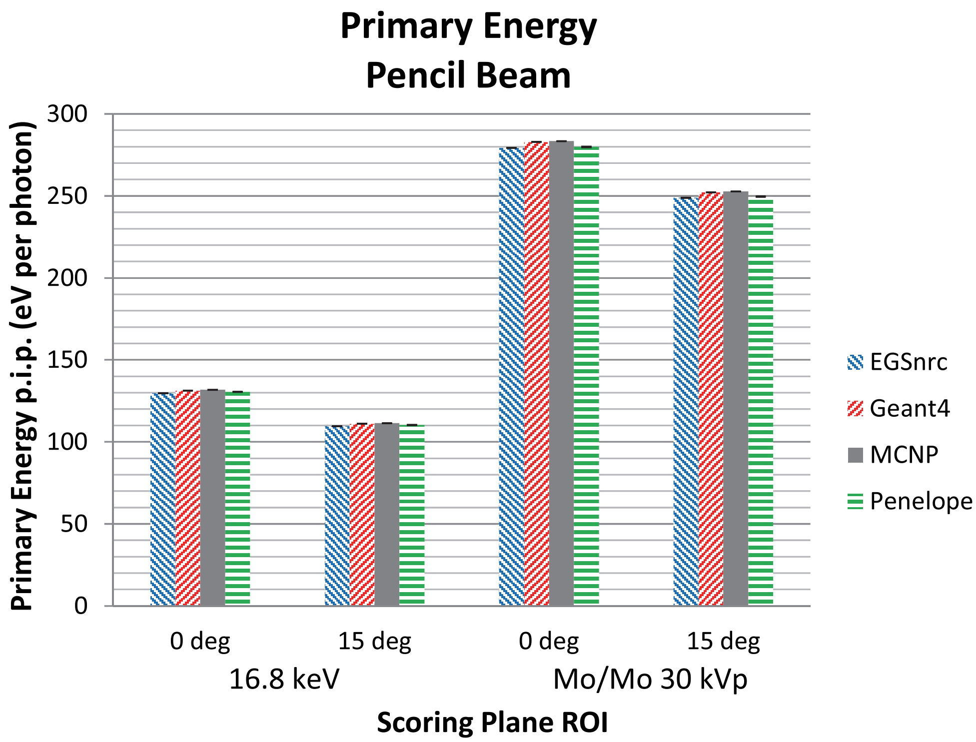

Figure 29. Primary only (both 0° and 15° projections) energy incident on the scoring plane ROI 5 per initial photon with the zero-area beam for both x-ray energies of Case #3 with the four Monte Carlo packages included in Table 2.

Table 20: Minimum and maximum ratios to the mean values for the primary energy incident in ROI 5 at the scoring plane for all Monte Carlo simulations performed for Case #3 with the zero-area x-ray beam. Statistical uncertainties are 0.03% to 0.13%.

	Mammography (0 deg)	Tomosynthesis (15 deg)
16.8 keV	0.991 – 1.008	0.991 – 1.008
Mo/Mo 30 kVp	0.993 – 1.007	0.993 – 1.007

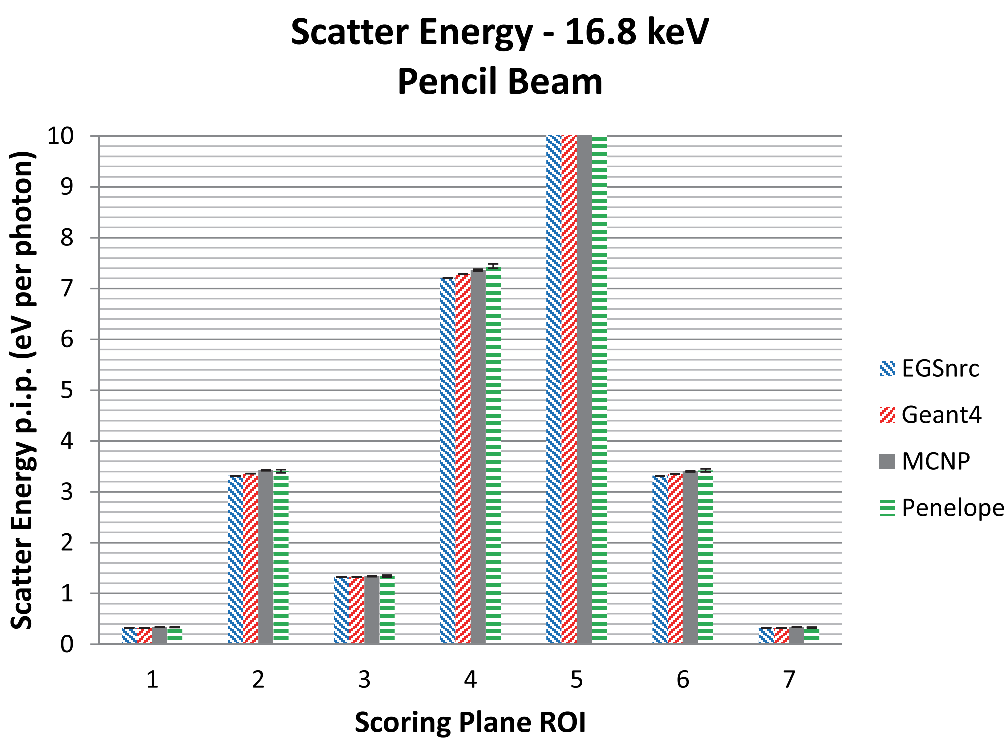

Figure 30. Scatter component of photon energy incident on the scoring plane ROIs per initial photon for the mammography (0° projection) 16.8 keV x-ray energy with the zero-area beam of Case #3 for the four Monte Carlo packages included in Table 2. Note that the columns for ROI 5 extend beyond the y-axis scale (to about 25 eV per initial photon), to enhance visibility of the results of the other ROIs.

Table 21: Minimum and maximum ratios to the mean values for the scatter component of the photon energy incident on each ROI at the scoring plane for all Monte Carlo simulations performed for Case #3 with the zero-area x-ray beam. Statistical uncertainties are 0.01% to 3.77%.

	16.8 keV		Mo/Mo 30 kVp	
Scoring Plane ROI	**Mammography (0 deg)**	**Tomosynthesis (15 deg)**	**Mammography (0 deg)**	**Tomosynthesis (15 deg)**
1	0.977 – 1.022	0.981 – 1.038	0.985 – 1.019	0.979 – 1.027
2	0.983 – 1.014	0.984 – 1.013	0.991 – 1.008	0.991 – 1.008
3	0.991 – 1.008	0.985 – 1.014	0.993 – 1.010	0.991 – 1.012
4	0.983 – 1.016	0.985 – 1.016	0.990 – 1.010	0.989 – 1.012
5	0.984 – 1.019	0.983 – 1.020	0.986 – 1.016	0.986 – 1.016
6	0.983 – 1.014	0.985 – 1.013	0.992 – 1.007	0.990 – 1.007
7	0.986 – 1.019	0.989 – 1.024	0.985 – 1.016	0.986 – 1.015

4.4 Case 4: Computed Tomography with Simple Solids

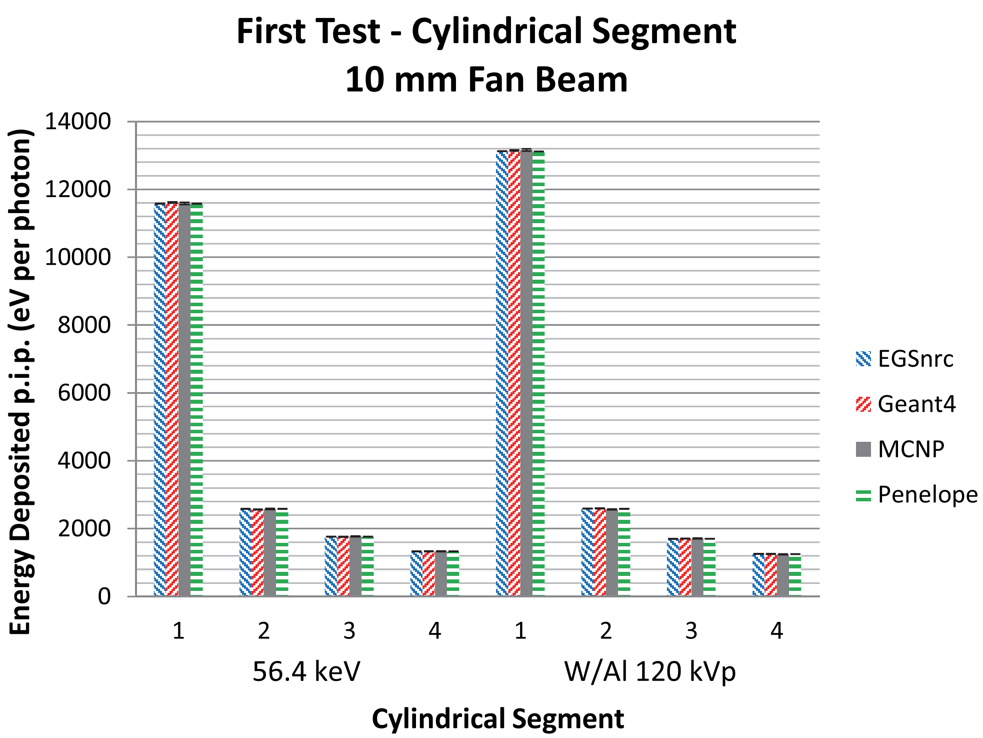

Figure 31. Energy deposited per initial photon in the four cylindrical VOIs of the phantom with the 10 mm thick fan beam of Case #4 for the four Monte Carlo packages included in Table 2.

Table 22: Minimum and maximum ratios to the mean values for the energy deposited in each of the four cylindrical VOIs of the phantom for all Monte Carlo simulations performed for the first test of Case #4. Statistical uncertainties are 0.02% to 0.79%.

	56.4 keV		W/Al 120 kVp	
Cylindrical VOI	Slice Thickness 10 mm	Slice Thickness 80 mm	Slice Thickness 10 mm	Slice Thickness 80 mm
1	0.999 – 1.002	0.997 – 1.002	0.998 – 1.002	0.997 – 1.003
2	0.995 – 1.002	0.998 – 1.001	0.994 – 1.003	0.995 – 1.005
3	0.996 – 1.004	0.995 – 1.003	0.997 – 1.003	0.994 – 1.005
4	0.999 – 1.001	0.989 – 1.006	0.995 – 1.004	0.988 – 1.006

Table 23: Minimum and maximum ratios to the mean values for the energy deposited in each of the two cylindrical VOIs of the phantom for all Monte Carlo simulations performed for the second test of Case #4 when using the random continuous x-ray source position. Statistical uncertainties are 0.27% to 0.81%.

	56.4 keV		W/Al 120 kVp	
Cylindrical VOI	Slice Thickness 10 mm	Slice Thickness 80 mm	Slice Thickness 10 mm	Slice Thickness 80 mm
Center	0.986 – 1.014	0.983 – 1.017	0.997 – 1.003	0.983 – 1.017
Perimeter	0.986 – 1.014	0.987 – 1.013	0.984 – 1.016	0.979 – 1.021

4.5 Case 5: Computed Tomography with a Voxelized Solid

Table 24: Minimum and maximum ratios to the mean values for the energy deposited in each organ/material in the voxelized volume representing the patient phantom for all Monte Carlo simulations performed for Case #5 when using the random continuous x-ray source position. These ranges include the results for Geant4 and MCNP, as listed in Table 2. Statistical uncertainties are 0.01% to 4.27%.

	Voxel Material															
	3 Soft Tissue	4 Heart	5 Lung	6 Liver	7 Gallbladder	8 Spleen	9 Stomach	10 Large Intestine	11 Pancreas	12 Adrenal	13 Thyroid	14 Thymus	15 Small Intestine	16 Esophagus	17 Skin	18 Breast	19 Cortical Bone
56.4 keV	0.994 – 1.006	0.999 – 1.001	0.998 – 1.002	0.998 – 1.002	0.994 – 1.006	0.997 – 1.003	0.998 – 1.002	0.999 – 1.001	0.999 – 1.001	0.961 – 1.039	0.988 – 1.002	0.989 – 1.011	0.998 – 1.002	0.996 – 1.004	0.992 – 1.008	0.995 – 1.005	0.996 – 1.004
W/Al 120 kVp	0.994 – 1.006	0.999 – 1.001	0.997 – 1.003	0.998 – 1.002	0.999 – 1.001	0.996 – 1.004	0.998 – 1.002	0.998 – 1.002	0.997 – 1.003	0.985 – 1.015	1.000 – 1.000	0.985 – 1.015	0.995 – 1.005	0.999 – 1.001	0.991 – 1.009	0.995 – 1.005	0.996 – 1.004

Table 25: Minimum and maximum ratios to the mean values for the energy deposited in each organ/material in the voxelized volume representing the patient phantom for all Monte Carlo simulations performed for Case #5 for the simulation with discrete x-ray source positions with the monoenergetic 56.4 keV source. Statistical uncertainties are 0.002% to 5.07%.

	Voxel Material																
Projection Angle	3 Soft Tissue	4 Heart	5 Lung	6 Liver	7 Gallbladder	8 Spleen	9 Stomach	10 Large Intestine	11 Pancreas	12 Adrenal	13 Thyroid	14 Thymus	15 Small Intestine	16 Esophagus	17 Skin	18 Breast	19 Cortica l Bone
0	0.999 – 1.002	0.996 – 1.008	0.997 – 1.006	0.995 – 1.010	0.994 – 1.014	0.996 – 1.009	0.994 – 1.012	0.993 – 1.016	0.994 – 1.012	0.957 – 1.030	0.988 – 1.005	0.985 – 1.006	0.992 – 1.017	0.994 – 1.009	0.999 – 1.001	0.992 – 1.018	0.998 – 1.003
45	0.999 – 1.002	0.996 – 1.008	0.997 – 1.005	0.995 – 1.010	0.988 – 1.023	0.996 – 1.010	0.995 – 1.010	0.985 – 1.018	0.994 – 1.011	0.963 – 1.016	0.993 – 1.006	0.986 – 1.008	0.995 – 1.011	0.997 – 1.005	0.999 – 1.001	0.989 – 1.024	0.998 – 1.004
90	0.999 – 1.002	0.993 – 1.014	0.995 – 1.008	0.995 – 1.012	0.994 – 1.012	0.991 – 1.015	0.992 – 1.017	0.995 – 1.012	0.993 – 1.017	0.974 – 1.049	0.984 – 1.014	0.993 – 1.004	0.997 – 1.005	0.994 – 1.012	0.999 – 1.001	0.995 – 1.009	0.996 – 1.009
135	0.994 – 1.003	0.997 – 1.005	0.998 – 1.002	0.997 – 1.005	0.996 – 1.006	0.993 – 1.006	0.998 – 1.004	0.998 – 1.004	0.999 – 1.002	0.974 – 1.037	0.996 – 1.004	0.984 – 1.006	0.993 – 1.005	0.998 – 1.002	0.994 – 1.003	0.990 – 1.004	0.995 – 1.002
180	0.998 – 1.002	0.993 – 1.015	0.996 – 1.008	0.994 – 1.011	0.985 – 1.027	0.994 – 1.012	0.995 – 1.011	0.992 – 1.017	0.998 – 1.004	0.993 – 1.005	0.995 – 1.007	0.995 – 1.009	0.992 – 1.016	0.995 – 1.011	0.999 – 1.001	0.984 – 1.031	1.000 – 1.001
225	0.995 – 1.003	0.997 – 1.003	0.998 – 1.002	0.996 – 1.007	0.985 – 1.013	0.997 – 1.005	0.997 – 1.003	0.998 – 1.002	0.995 – 1.004	0.988 – 1.006	0.996 – 1.003	0.989 – 1.010	0.997 – 1.004	0.996 – 1.006	0.996 – 1.002	0.994 – 1.014	0.996 – 1.002
270	0.998 – 1.003	0.994 – 1.013	0.996 – 1.008	0.995 – 1.015	0.978 – 1.040	0.995 – 1.013	0.995 – 1.013	0.991 – 1.021	0.993 – 1.014	0.950 – 1.062	0.990 – 1.025	0.998 – 1.002	0.994 – 1.008	0.995 – 1.010	0.999 – 1.002	0.989 – 1.026	0.996 – 1.009
315	0.995 – 1.002	0.998 - 1.003	0.998 – 1.002	0.997 – 1.005	0.996 – 1.005	0.997 – 1.009	0.995 – 1.007	0.992 – 1.008	0.992 – 1.007	0.987 – 1.013	0.991 – 1.010	0.985 – 1.006	0.994 – 1.007	0.998 – 1.001	0.995 – 1.003	0.994 – 1.012	0.996 – 1.002

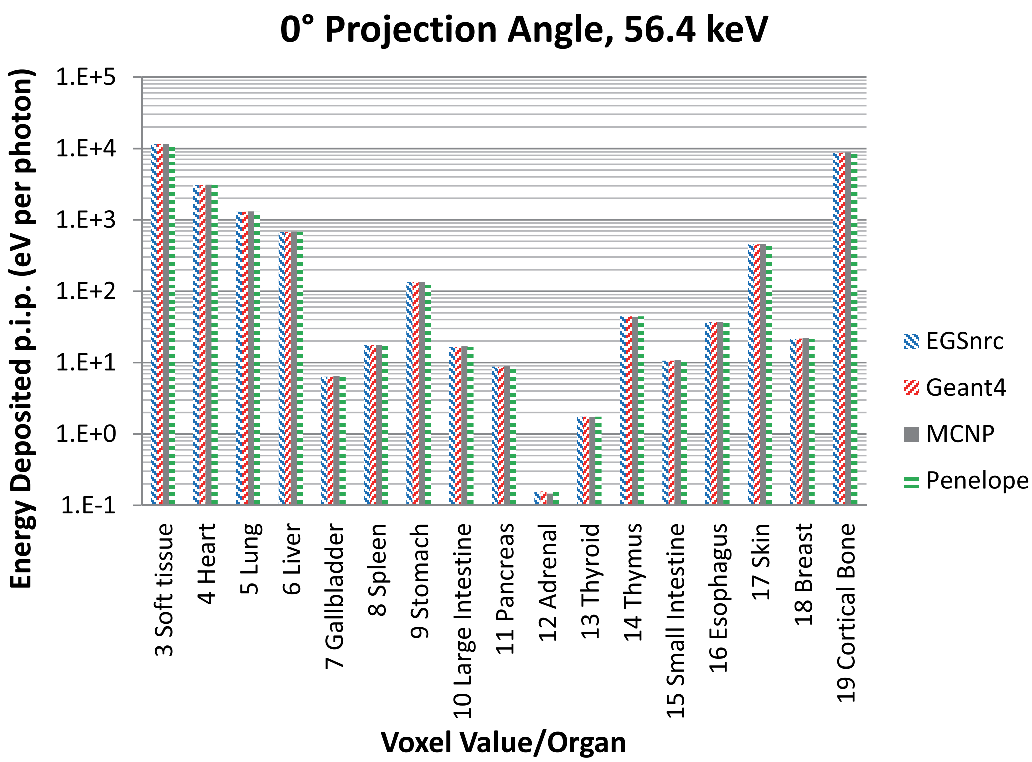

Figure 33. Energy deposited per initial photon in the voxelized phantom with the 10 mm thick fan beam and the 56.4 keV x-ray energy at the 0° projection angle only of Case #5, for the four Monte Carlo packages included in Table 2.

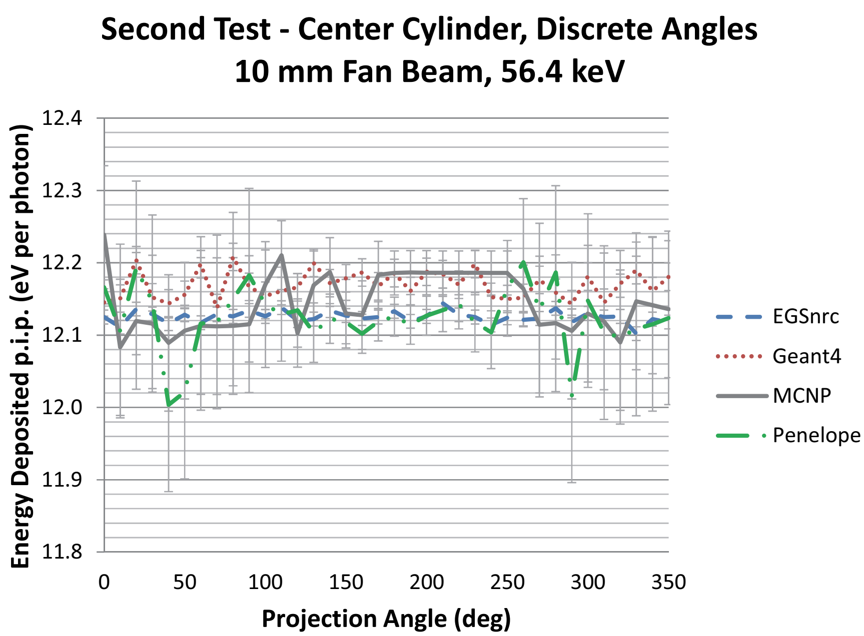

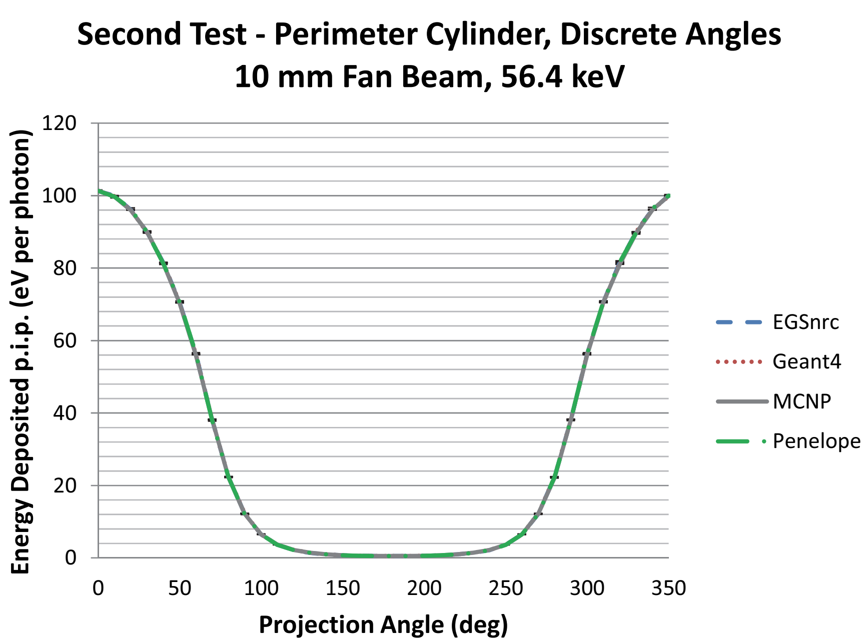

Figure 32. Energy deposited per initial photon in center (top) and perimeter (bottom) cylindrical VOI of the phantom with the 10 mm thick fan beam and the 56.4 keV x-ray energy of Case #4 for the four Monte Carlo packages included in Table 2. Note the very narrow range of the vertical scale of the top graph, showing the similarity among all results.

4.6 Case 6: X-ray Production

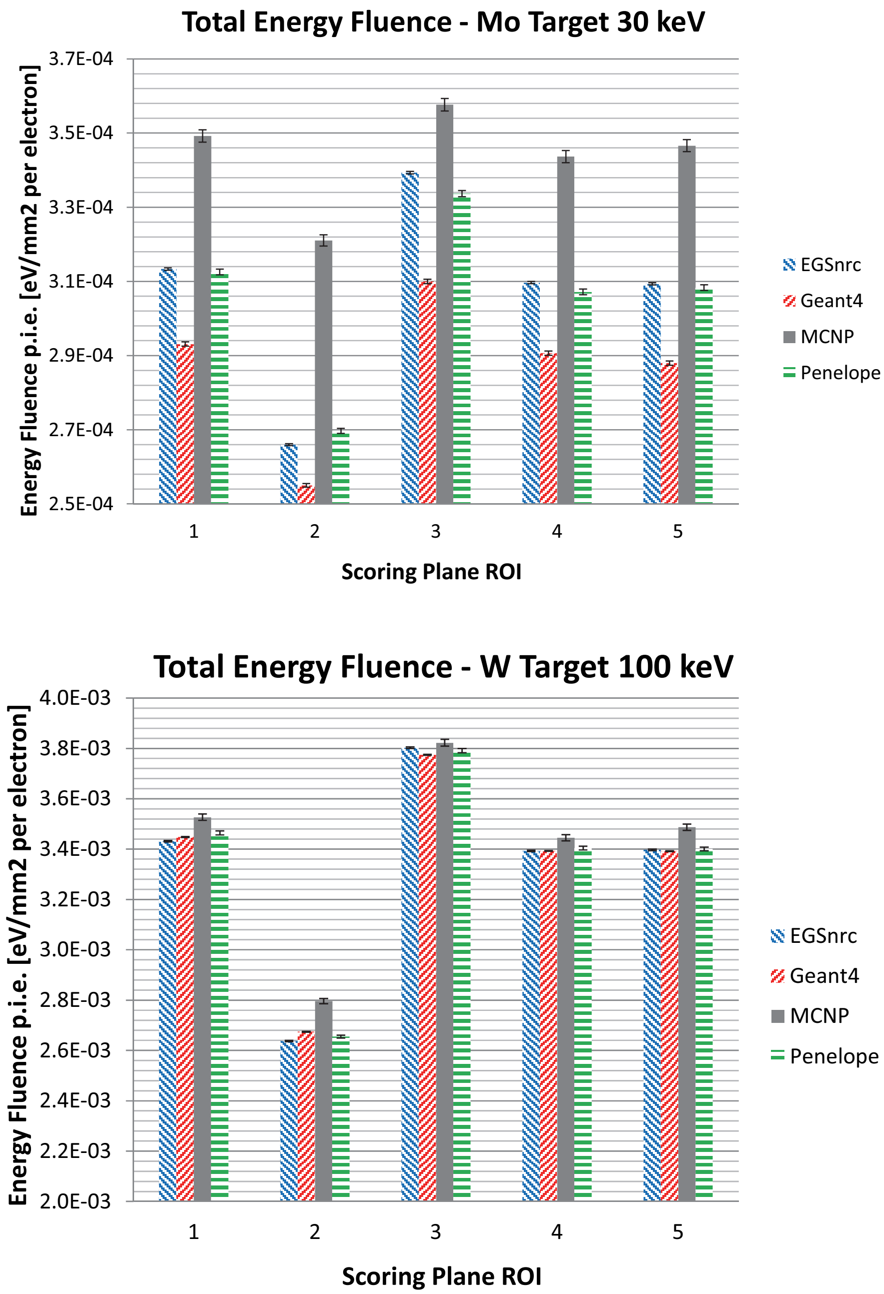

Figure 34. Total energy fluence per initial electron at the scoring plane for the Mo target (top) and W target (bottom) simulations of x-ray production of Case #6 for the four Monte Carlo packages included in Table 2.

Table 26: Minimum and maximum ratios to the mean values for the planar energy fluence at the scoring plane for all Monte Carlo simulations performed for Case #6. Statistical uncertainties are 0.05% to 0.47%.

	ROI 1	ROI 2	ROI 3	ROI 4	ROI 5
Mo target, 30 keV	0.924 – 1.101	0.918 – 1.155	0.925 – 1.067	0.929 – 1.099	0.920 – 1.107
W target, 100 keV	0.990 – 1.017	0.980 – 1.039	0.994 – 1.007	0.995 – 1.011	0.992 – 1.020

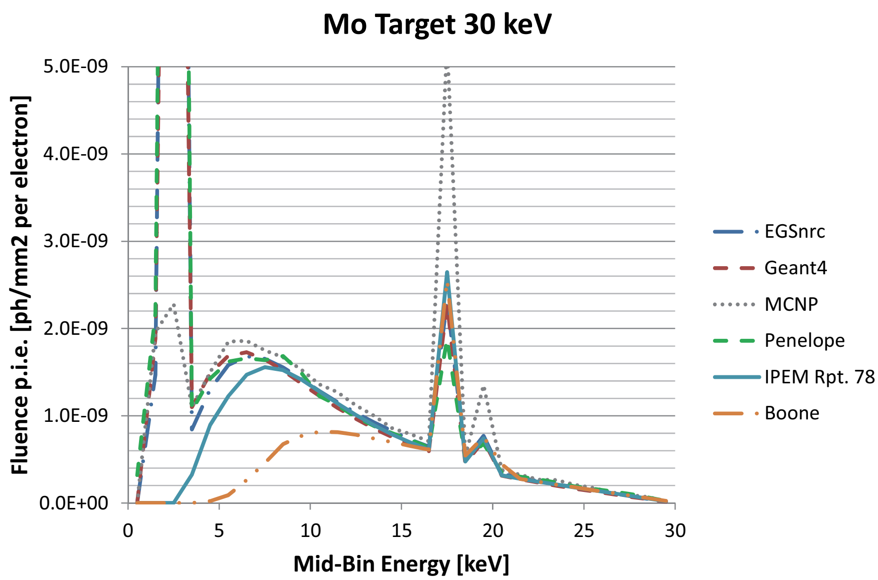

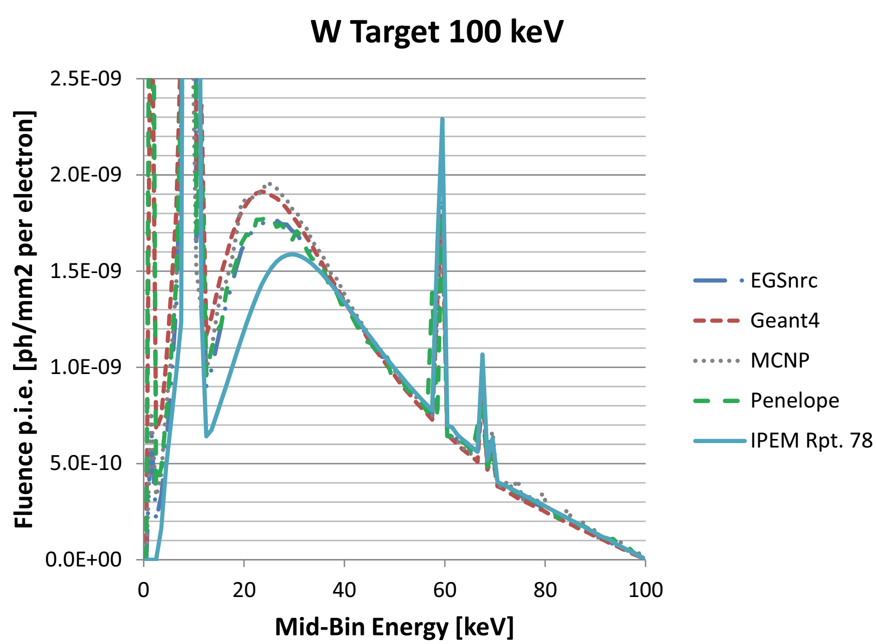

Figure 35. Photon fluence spectrum per initial electron in ROI 1 for 30 keV electrons on the Mo target (top) and 100 keV electrons on the W target of Case 6 for the four Monte Carlo packages included in Table 2 and as estimated by two spectrum models.[24,27] The two spectra models include some inherent filtration, so differences at low x-ray energies are not relevant.

Table 27: Relative energy fluence at ROI 1, 2, and 3 (setting the central ROI [#1] as 100%) showing the heel effect for the four Monte Carlo packages included in Table 2

Mo Target ROI	EGSnrc	Geant4	MCNP	Penelope
3	108.3%	105.8%	102.4%	106.8%
1	100.0%	100.0%	100.0%	100.0%
2	84.9%	87.0%	91.9%	86.3%
Uncertainty	0.14%	0.28%	0.66%	0.35%
W Target ROI	**EGSnrc**	**Geant4**	**MCNP**	**Penelope**
3	110.8%	109.5%	108.4%	109.4%
1	100.0%	100.0%	100.0%	100.0%
2	76.9%	77.6%	79.3%	76.6%
Uncertainty	0.13%	0.07%	0.51%	0.31%

5. Discussion

5.1 Comparison of Results among Monte Carlo Packages

In general, the implementations of all six cases with the four Monte Carlo packages included in this report resulted in estimates with very good concordance, with most of the results being within the statistical uncertainty of the simulations. For those differences that exceeded the statistical uncertainty, many differences are within ~5% and most within 10% of the mean of the results. Some, if not all, of the differences beyond statistical uncertainty could be due to small differences in interpretation of the simulation conditions or even errors in implementation of the cases by the task group members. Every attempt was made to minimize this possibility. In some of the cases, the differences were also clearly produced by the underlying differences in the physical models used by the multiple codes, such as small differences in the energy of the emitted characteristic x-ray or the modeling of Compton scattering events.

In the electronic version of the results available for download, the results of each implementation are provided to allow the readers to analyze the case-by-case concordance for any of the results in detail. Here we present a summary of the findings:

5.1.1 Case 1: Half Value Layer

The estimated primary and total planar fluence values for all simulations among all four Monte Carlo implementations matched well, and the resulting air kerma ratios were all very close to the expected values of 0.500 and 0.250 for the HVL and QVL, respectively.

The thicknesses of the aluminum filter included in the case description were calculated analytically using the NIST XCOM dataset.[21] Therefore, it was expected that the Monte Carlo packages that use the same cross-section databases, such as GEANT4 and MCNP, would yield air kerma ratios very close to 0.5 and 0.25 for the half and quarter value layer thicknesses, respectively. Since EGSnrc (default) and Penelope incoherent scattering model is based on the Relativistic Impulse Approximation (RIA)[13,28–30], their Compton cross sections are different from those in the NIST XCOM dataset. As a consequence, their half and quarter value layers differ from the expected values by a small but statistically significant difference (see Table 28). In order to reproduce the expected values, EGSnrc calculations were run in a NIST-like mode by using XCOM Compton cross sections (see Section A in the Appendix)[31]. In this mode, the values obtained are much closer to the expected values.

Table 28: Comparison of EGSnrc and Penelope values of the HVL and QVL for 100 keV photons calculated taking into account the primary photons only (R1 and R2). Statistical uncertainties of these results are 0.006% and 0.000035% for Penelope and EGSnrc values, respectively.

	HVL (primaries only) R_1	QVL (primaries only) R_2
EGSnrc (NIST)	0.49973	0.24973
EGSnrc (default)	0.49792	0.24793
Penelope	0.49781	0.24721

5.1.2 Case 2: Radiography and Body Tomosynthesis

The dose results for all codes and both projection angles yielded very similar results, with almost all estimates well within 2% of each other. The x-ray scatter study also shows excellent agreement among all codes at the 2% level. The only notable deviation from this excellent agreement was found to be for the single Compton scatter estimate of the ROI #5 in the zero area beam simulations (this result can be found in the electronic version of the results). For this particular ROI, the value obtained with Penelope is 6% and 8% larger than the value from EGSnrc and Geant4, respectively. This ROI is the one toward which the beam was directed, so scoring this quantity involves the estimation of very narrow-angle Compton scattering. It is possible that there is a larger variation in the physics models among the packages for this physical interaction, but the cause for these larger discrepancies for this ROI requires further investigation and is beyond the scope of this report.

As in Case 1, the use of different Compton scattering models by the different Monte Carlo codes has an impact on the resulting primary x-ray energy incident on the detector. Although the differences shown in Figures 23 and 24 are small, (2.4% to 3.6% for the full field and 2% to 3% for the pencil beam), it can be seen in Figure 36 that results obtained with EGSnrc using a NIST-like physics model

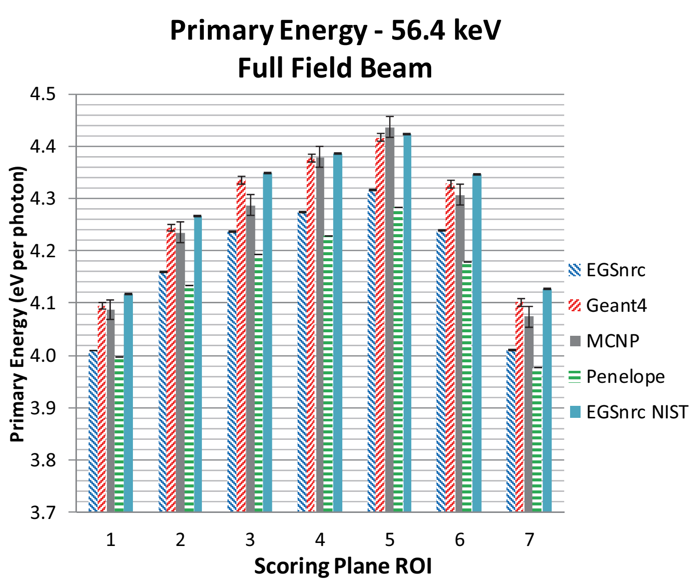

Figure 36. Effect of two different photon physics models on the primary energy incident per incident photon on the scoring plane with the full-field 56.4 keV x-ray beam for the radiography (0° projection) simulation of Case #2.

are closer to Geant4 and MCNP results, while EGSnrc results using default parameters for Compton scattering are closer to Penelope results.

The mono-energetic primary photon beam reaching the scoring plane is very sensitive to differences in the photon cross sections since it is directly proportional to $e^{-\mu x}$, where μ is the total photon cross section and x is the photon path length in the attenuating material. For this 20 cm thick phantom, a 1% change in μ translates into a greater than 4% change in $e^{-\mu x}$.

5.1.3 Case 3: Mammography and Breast Tomosynthesis

In general, the dose results for all codes, projection angles, monoenergetic and spectral simulations, and both beam types yielded very similar results, with almost all estimates well within 2% of each other. Again, the estimation of narrow-angle Compton scattering appears to show a larger variation in the physics models (see variation in ROI #5 for the zero area beam). At the lower energies used in this simulation, the full-field estimation of Compton scatter also yields larger differences than the other estimates. Therefore, the Compton scatter models show greater variability at both narrow scatter angles and low x-ray energies.

5.1.4 Case 4: Computed Tomography with Simple Solids

Practically all results from all four Monte Carlo packages were found to be within the statistical uncertainty.

5.1.5 Case 5: Computed Tomography with Voxelized Solid

Except for the adrenals, for which the dose estimates had larger statistical uncertainty, the results for the energy deposition for practically all other organs for both the random and discrete projection angles yielded very similar results, within 1% to 2% for all codes.

It is worth noting that the estimation of the radiation dose deposited inside the voxels of computational human phantoms is one of the most relevant and common types of simulation performed in medical physics research. The results obtained highlight the precision and reliability of dosimetric studies performed with Monte Carlo simulation codes. As expected, the estimation of dose deposition inside millimeter-sized voxels is not very sensitive to the differences in the physics used by different codes.

5.1.6 Case 6: X-Ray Production

This simulation case is more sensitive to subtle differences in physics models compared to the other simulations because it is sensitive to electron transport details. Thus it is to be expected that the comparison among the different Monte Carlo simulation packages would be the most challenging. Differences among the predicted energy-discriminated fluence were found to be approximately ±10% to 20%, except for the very low-energy bins below approximately 3 keV for the Mo spectrum and 12 keV for the W spectrum, respectively. At these very low energies, where the electron interaction physics models are known to have larger uncertainties, the discrepancies between codes were considerably larger. At these energies, however, diagnostic imaging conditions normally result in these x-rays being fully attenuated by added x-ray tube filtration, so these discrepancies should not impact realistic imaging research. It should be noted that the results with MCNP resulted in characteristic emission peaks for the Mo target that were substantially higher than those predicted by the other codes.

While the total energy fluence estimates for the W target spanned a range of approximately ±1% to ±2%, with only one difference being 4%, the Mo target spectrum simulations demonstrated much larger differences, mostly due to the substantially higher estimates in characteristic emission by the MCNP simulations. These calculations are sensitive to the electron impact ionization cross sections used.

5.2 Lessons learned

The exercise performed for this task group report, specifically the design and implementation of several simulation test cases with a number of different Monte Carlo simulation packages, resulted in a number of problems that were identified and corrected along the way. These problems and inconsistencies in interpretation now provide information that we hope will help readers when implementing their own Monte Carlo simulations.

Chief among the problems that could be encountered is that the specifications of the simulations may not be followed accurately. Preliminary results of some of the cases included in this report resulted in large differences among the codes which had to be identified and corrected until the task group was confident that remaining discrepancies were present either due to statistical uncertainties or real differences in either the physics tables of each package or some other aspect inside each code. An example of actual differences in the codes is the small difference in the energy of some characteristic emission x-rays which resulted in associated peaks corresponding to different energy bins depending on the Monte Carlo package used. Therefore, utmost care should be taken in implementing these simulations with the correct input parameters in terms of geometry, materials, source, and scoring. Errors observed during this exercise, and that can be easily repeated, include the following:

1. Incorrect source type (e.g., isotropic vs. non-isotropic point source). For all simulations except Case 6 and the point spread function sources (cases 2 and 3), the source should be isotropic.
2. Incorrect scoring metric (e.g., fluence vs. planar fluence vs. energy fluence). For comparison to the present data, all fluence scoring should be planar fluence, i.e., the cosine factor does not apply.
3. Incorrect scoring units (e.g., total x-rays incident in an ROI vs. x-rays/mm^2). Care should be taken in using the same units as those shown in the provided results spreadsheets.
4. Incorrect binning (e.g., does the energy of a bin represent the mid-level, minimum, or maximum of a bin? All spectral information, i.e., the x-ray spectra provided for the simulations and the results for cases 1 and 6 specify the mid-level of the energy bin.
5. Incorrect material composition and density definition. Care should be taken when defining the materials.
6. Direction of travel in rotating/translating sources. The directions in which rotations or translations are positive are marked in the figures.
7. X-ray source translation vs. rotation. Note that to more accurately reflect the way the corresponding imaging systems function, the simulation of body tomosynthesis calls for the x-ray source to translate parallel to the scoring plane to an angle of 15°, while the simulation of breast tomosynthesis involves the source rotating about a point at the scoring plane to an angle of 15°.
8. Incorrect normalization. All results normalized "per photon history" are normalized to only the acceptable histories that are emitted toward the area specified (in most cases, the entire scoring plane). The results should not be normalized to all histories potentially emitted in all directions covering the 4π sphere. The EGSnrc collimated source gives quantities normalized to the incident real fluence, not the number of histories. To convert to a quantity normalized per number of particles, one has to calculate the solid angle subtended by the point source and the scoring plane.
9. Excluding the surrounding air was found to have a non-negligible effect on the results in cases 1 and 4.

One issue that can introduce differences in the results is the setting of the energy or range threshold/cut. This is a very important parameter in many simulations, and it can have a substantial impact on the results in many types of Monte Carlo simulations. Among the cases included in this report, this is especially true for Case #6, the simulation of the generation of x-rays.

An interesting issue was observed with MCNP for Case #4. For all simulations for this case, a void collimator (material of the collimator set as a void region where photons have no importance) was used to properly collimate the isotropic x-ray point source. When the collimator and point source were rotated in 10° increments about the phantom, large differences between results for MCNP and the other codes were observed between 60–80° and 280–300°. These differences were eliminated when the phantom inserts, not the collimator and point source, were rotated in 10° increments. It appears that the rotation of a rigid shape (like the collimator assembly) in an environment with some finite spatial resolution may result in unexpected behavior when photons interact with the edges of the rotated, rigid structure. Although no clear explanation is available to account for this observation, care should be taken, at least with MCNP, when using a rotated collimator assembly.

Finally, care should be taken when incorporating variance reduction techniques in the simulations. During the early stages of obtaining the results for this report, a bug in the implementation of the variance reduction technique of “particle splitting” in Geant4 version 9.5 and 9.5 patch 1 was found. Due to this bug, the reduced weight given to each split photon was not inherited by any subsequently created secondary particle by these photons, resulting in biased results. This was only identified during the comparison of the results of the different packages performed during this work, but could have gone unnoticed in regular research work. The bug has been corrected in later versions of Geant4, including the one used in the final simulations of all cases included in this report (version 9.6 patch 2).

5.3 Simulation Times

It was not the goal of this task group to compare the efficiency of the Monte Carlo packages tested, but rather to provide consistent results among them, with the priority being that the simulation conditions be as similar to each other as possible. Therefore, the use of the most efficient methods to perform these simulations, including the use of variance reduction techniques, varied considerably among the groups implementing the simulations. For example, the Penelope simulations were not run with any variance reduction techniques, and the simulations included the tracking of electrons, although their inclusion is not expected to affect the results. Although it was not always the case, some of the other implementations did include variance reduction and did not include tracking of electrons. This resulted in the Penelope simulation times being larger in general than those for the other codes. The specific simulation parameters used in the implementation of all cases for each Monte Carlo package are provided in the Appendix.

In the interest of disseminating as much information as possible, however, we have included in each results spreadsheet some timing information. Specifically, the spreadsheets include the average time taken per single history simulated and the amount of time that would be taken by a single, modern CPU to achieve a 1% statistical uncertainty for a single or a number of scored quantities per case. Which scored quantity is the one that the timing to 1% precision is referred to is marked in the spreadsheets by a color highlight. These timing data should only serve as a rough guide, since they were not produced on the same computer and, as mentioned above, the efficiency of the simulations was not a priority. In addition, estimating the timing to 1% precision from simulation times that resulted in scores with orders of magnitude higher precision may result in a substantial underestimation of required simulation time. However, useful observations can be made. In particular, in various situations, variance reduction techniques have the ability to very substantially improve the efficiency of calculations. For example, a factor of 2,000x improvement was obtained in the efficiency of the EGSnrc calculations in case #6 (x-ray spectra) by using variance reduction techniques. While using variance reduction methods that are part of general purpose code systems, one must take great care when implementing them in a new code and verify their accurate implementation by comparison to runs with the technique turned off.

6. Conclusion

This task group developed and implemented six simulations of typical experiments performed for diagnostic imaging research with x-rays. These simulations were implemented with four different well-known and publicly available Monte Carlo packages, and the results were compared. All details of the inputs and the outputs to the simulations are provided in this report and in associated electronic files.

It is the intent of this task group to provide researchers who are using Monte Carlo simulations with a standardized methodology to validate their simulations before embarking on research. We believe that providing these data will eliminate the need to (a) search the literature for potential comparable simulations, (b) make informed decisions of the many details that are normally not included in scientific articles, (c) obtain numerical data from published graphs, and (d) contact publication authors in hopes of gaining more information on the relevant inputs and results of simulations performed, in some cases, many years ago.

Of course, each research investigation has different requirements, and therefore the Monte Carlo simulations needed may include higher levels of complexity compared to those presented in this report. For example, the simulations described in Case 3 (mammography and breast tomosynthesis) may be completely sufficient for investigations of dose in a homogeneous breast. On the other hand, Case 5 (computed tomography dosimetry with a voxelized patient model) may not be sufficient to estimate dose to patients from helical CT scans using automatic exposure control techniques or with the presence of a complex bow-tie filter. If higher levels of complexity are required, then it is up to the investigator to determine which additional validation steps would be needed (e.g., comparisons with physical measurements). Even in these situations in which the cases presented here are not sufficient for complete validation, comparisons to the reference cases described in this report are strongly recommended. Therefore, this task group recommends the following:

1. All Monte Carlo methods used for medical imaging research for publication in scientific journals be analyzed by comparing results obtained with the proposed methods to results of the relevant case(s) included in this report.
2. The analyses be included in published and presented works, with a reference to the specific case used, and a description of the relevant details of the case, including x-ray spectra, imaged objects, tallies performed, and statistics of the Monte Carlo results, as well as the relative percentage difference found between the results obtained and the corresponding mean of the results in this report. If the results obtained are outside the ranges of results presented in this report, the relative percentage deviations from these ranges also need to be provided and justified.
3. This task group suggests the following language to describe the comparison: "The Monte Carlo methods used in this work were tested by performing case(s) XX-YY of the American Association of Physicists in Medicine Task Group Report 195 *(ref)*. The simulations were performed using … *(provide details of simulation as listed in point 2 above)*. The results of our simulations agree to within X% of the mean results published by TG-195 and they *(either)* fall within the range of results published by TG-195 *(or)* are Y% from the lower/upper limit of the range of results published by TG-195. The statistical uncertainty obtained for these simulations was Z%." A table listing the detailed results of this analysis with appropriate uncertainty estimates is preferred.
4. In published and presented works, the Monte Carlo code and methods being used be described in detail including software and hardware, total computation time, and any optional parameters being

used (e.g., variance reduction techniques, energy cutoff values). Any relevant modification of the standard code release (such us a new scoring routine) should be described with enough detail that it could be reproduced by independent investigators.

5. In published works, reference to this report should be made by including a citation to the paper describing this task group report in the journal *Medical Physics*.

This task group report can also be useful as an educational tool for trainees and scientists gaining experience in the field of Monte Carlo simulations, either as a self-teaching tool to ensure that he/she is able to correctly perform a specific simulation, or as assigned learning projects as part of course objectives or training programs.

Of course, many imaging modalities and potential simulation types are not included in this report. This first undertaking had to be limited to a manageable number of cases to be completed in a realistic time frame. In the future, similar reports that include simulations of other types of measurements or other imaging modalities may be published by the AAPM.

7. Acknowledgments

The task group would like to thank Samir Abboud, Cecilia Marini Bettolo, Bahaa Ghammraoui, Sebastien Incerti, Vladimir Ivantchenko, Alfonso Mantero, Luciano Pandola, Joseph Perl, and Yakun Zhang for their contributions to this work. We thank Eric Jablonowski for his contributions to the figures. This work was supported in part by the U.S. Department of Energy under contract number DE-AC02-76SF00515.

APPENDIX:

Monte Carlo Package-specific Simulation Parameters

The following is a listing of the specific simulation parameters for the different Monte Carlo packages used to obtain the results included in this report. Depending on the requirements of each package, the number and type of parameters can and do vary widely.

A. EGSnrc

1. All cases were simulated with EGSnrc April 2013 release V4-r2-4-0.
2. Photons were followed down to 1 keV, and no electron transport was included in the simulations except in Case 6, where electrons were followed down to 1 keV. Default Monte Carlo transport parameters were used for all cases, except for Case 1 where NIST XCOM Compton photon cross sections were used to better match expected HVL and QVL values.

   For case 6, x-ray production, the default electron impact ionization cross section by Kawrakow was used, although using the Penelope cross section option[32] increased the total photon fluence by 6% or 7% for the Mo target case, and the fluorescent peaks by much more.
3. The user-code cavity was used in HVL calculation mode for Case 1, and tutor7pp was used for cases 2 and 4. For the mammography case (Case 3), the user-code egs_mammo was derived from tutor7pp to allow for glandular dose and solid angle calculations. Ausgab scoring object egs_dose_scoring was developed to score dose in cases 4 and 5. A C++ version of ctcreate, ctcreate_raw, was developed that allows creation of egsphant files from a raw binary image. The BEAMnrc user-code was used to model x-ray production from W and Mo targets (Case 6). For this case, spectral distribution, particle, and energy fluences were obtained in two different ways, one using beamdp and a phase-space file, and another using cavity and a newly developed ausgab scoring object egs_fluence_scoring. Both approaches produced identical results within statistical uncertainties.
4. Variance reduction techniques were used to increase the efficiency of the simulations. Photon emission from point sources into a specific scoring field (cases 2, 3, 4, and 5) was simulated using a collimated source algorithm, uniformly sampling directions to the scoring field and adjusting the statistical weight accordingly to account for the spatial dependency of the point source photon fluence (EGS_CollimatedSource from the EGSnrc C++ class library). Directional Bremsstrahlung Splitting (DBS)[33,34] and Bremsstrahlung Cross Section Enhancement (BCSE)[3] increased the efficiency of x-ray spectra calculations (Case 6) with BEAMnrc. Forced detection was turned on in cavity for HVL calculations, allowing a very efficient ray-tracing from the source to the scoring field.
5. The collimated source used with EGSnrc (particles are only emitted in the scoring field direction), combined with the forced detection scoring scheme, gives the right answer even with one history for a mono-energetic source. This is equivalent to an analytical ray-tracing, and because the solid angle subtended by the scoring field and the source is very small, the maximum variation that one can get is 0.0005% and 0.0008% with two histories for the 0 cm and thickest filter, respectively. As a consequence, the statistical uncertainty reported for several million histories is extremely small, and the 1% statistical uncertainty is just unreachable using this approach. On the other hand, if one were to use an isotropic source, then the time needed for a 1% statistical uncertainty in the primary fluence would be 865 sec.

6. Statistical uncertainties were calculated using the "history by history" methods detailed by Walters et al.[35]

B. Geant4

1. All cases simulated with the Geant4 toolkit for Monte Carlo simulations used version 9.6 patch 2 of the package.
2. All cases were simulated with the electromagnetic physics option 4 package, except for Case 6, for which the Livermore electromagnetic physics package was used.
3. For all cases except case #6, the cut values used for all particles were the default ones used by this physics package. For Case #6, the cut values were set to 1.0 μm and a low edge of 1.0 keV.
4. In all cases, electron transport was simulated, although this was not needed except in Case #6.
5. In all cases but Case #6, no variance reduction methods were used. For Case #6, the uniform Bremsstrahlung splitting algorithm provided in this version of Geant4 was used. It was confirmed that the results were not biased by this method.
6. No pre-programmed sensitive detectors included in the toolkit were used for these simulations; for each case, the required sensitive detector was created with custom-made code.
7. For Case #5, the voxelized navigation was performed with the Nested Parameterisation option.
8. All elements were built using the provided NIST material manager, with the compounds defined from these elements as specified in this report.
9. Statistical uncertainties for all scoring was performed by implementing the method described by Sempau et al.[36]

C. MCNP

1. All cases were simulated using MCNPX v2.7a.[17]
2. Electron transport was simulated only in Case #6.
3. Within all the simulations, the detailed photon transport mode with a low-energy cutoff of 1 keV was used. The detailed physics treatment included coherent scattering and accounted for fluorescent photons after photoelectric absorption. Form factors and Compton profiles were used to account for electron binding effects. The incoherent, coherent, and photoelectric cross-section data are based on ENDF/B-IV.[37]
4. For all cases involving dose calculations, simulation physics options were set so that the photon transport mode does not explicitly create photoelectrons, but instead assumes all secondary electrons deposit their energy at the photon interaction site, which is reasonable given the incident photon energy distribution. This assumption satisfies charged particle equilibrium and allows absorbed dose to be approximated as collision kerma, which was calculated in each volume of interest by tallying the photon energy fluence and multiplying by the material-specific and energy-dependent mass energy-absorption coefficient.[21]
5. Modifications were made to the standard MCNPX source code in order to randomly sample the angular position of the x-ray source in cases 4 and 5.

D. Penelope

1. All simulations were performed using PENELOPE 2006 (except for case 6, which used PENELOPE 2008) and the penEasy main program.[18–20] The variance reduction methods included in penEasy were not used, and no particular effort was made to optimize the simulation speed to avoid compromising the accuracy of these reference results. The user-defined parameters that con-

trol the accuracy of the PENELOPE electron and photon transport routines were conservatively chosen to produce reliable results, even if the simulation speed was reduced. The cut-off energies for simulating transport of electrons and photons were separately determined for each simulation depending on the detector system used. For example, in Case #5, the absorption energies were quite large, 30 keV for electrons and 5 keV for photons, because the scoring volumes were big compared to the residual range of particles at these energies. In the cases that required an accurate simulation of low-energy radiation, such as the half value layer estimation and the x-ray production, a detailed simulation down to 1 keV for electrons and 0.5 keV for photons was performed.

2. The specific version of the penEasy main program used in this study was penEasy_Imaging, an extension of penEasy for the study of medical imaging applications (free software is available at http://code.google.com/p/peneasy-imaging/). To reduce the time required to complete the simulations, the main program was modified to use the MPI libraries to execute the simulations in parallel in a cluster of computers. The most time-consuming cases were executed in parallel in more than 200 CPU cores to obtain the results in a reasonable amount of time. It was confirmed that the results of the parallel executions and sequential runs with the same random number seeds were identical.

3. Some of the simulated cases required small modifications of the main program to score the parameters of interest in the way specified in the case description. In particular, the fluence estimation tally defined in penEasy was not used to estimate the fluence because of the use of different definitions for this magnitude. In most cases, Python scripts had to be developed to post-process the simulation output and obtain the desired data in the appropriate format. It was in the post-processing and data collection step where the majority of user errors were made while preparing the preliminary results for this report. The availability of benchmark data from other groups was essential to detect seemingly trivial errors, such as inadequate normalization, wrong units, geometric errors in the location of the volumes of interest, or the use of incorrect material files. Some of these errors resulted in orders of magnitude errors in the results that could have been overlooked in normal situations, but were easily fixed after the benchmark.

References

[1]J. R. Mercier, D. T. Kopp, W. D. McDavid, S. B. Dove, J. L. Lancaster, and D. M. Tucker, "Modification and benchmarking of MCNP for low-energy tungsten spectra." Med. Phys. **27**, 2680–2687 (2000).

[2]G. A. P. Cirrone, et al. "Precision validation of Geant4 electromagnetic physics." In *Nuclear Science Symposium Conference Record, 2003 IEEE*, (2003), vol. 48, p. 482–485.

[3]E. S. Ali and D. W. Rogers. "Efficiency improvements of x-ray simulations in EGSnrc user-codes using bremsstrahlung cross-section enhancement (BCSE)." Med. Phys. **34**, 2143–2154 (2007).

[4]C. M. Salgado, C. C. Conti, and P. H. B. Becker. "Determination of HPGe detector response using MCNP5 for 20–150 keV X-rays." Appl. Radiat. Isot. **64**, 700–705 (2006).

[5]S. España, J. L. Herraiz, E. Vicente, J. J. Vaquero, M. Desco, and J. M. Udias, "PeneloPET, a Monte Carlo PET simulation tool based on PENELOPE: features and validation." Phys. Med. Biol. **54**, 1723 (2009).

[6]A. Loehr, J. Durst, T. Michel, G. Anton, and P. Geithner. "Comparison of recent experimental data with Monte Carlo tools such as RoSi, Geant4 and Penelope." In *Nuclear Science Symposium Conference Record (NSS/MIC), 2009 IEEE*, (2009), p. 3904–3908.

[7]M. Batic, G. Hoff, M. G. Pia, and P. Saracco. "Photon Elastic Scattering Simulation: Validation and Improvements to Geant4." IEEE Trans. Nucl. Sci. **59**, 1636–1664 (2012).

[8]K. Sangroh, T. Y. Terry, Y. Fang-Fang, and J. C. Indrin. "Spiral computed tomography phase-space source model in the BEAMnrc/EGSnrc Monte Carlo system: implementation and validation." Phys. Med. Biol. **58**, 2609 (2013).

[9]G. Weidenspointner, Batic, x, M., S. Hauf, G. Hoff, M. Kuster, M. G. Pia, and P. Saracco, "Validation of Compton scattering Monte Carlo simulation models." In *Nuclear Science Symposium and Medical Imaging Conference (NSS/MIC), 2013 IEEE*, (2013), p. 1–5.

[10]R. Schmidt, J. Wulff, and K. Zink. "GMctdospp: Description and validation of a CT dose calculation system." Med. Phys. **42**, 4260–4270 (2015).

[11]D. W. O. Rogers, B. A. Faddegon, G. X. Ding, C. M. Ma, J. We, and T. R. Mackie. "BEAM: a Monte Carlo code to simulate radiotherapy treatment units." Med. Phys. **22**, 503–524 (1995).

[12]I. Kawrakow, "Accurate condensed history Monte Carlo simulation of electron transport. I. EGSnrc, the new EGS4 version." Med. Phys. **27**, 485–498 (2000).

[13]I. Kawrakow, E. Mainegra-Hing, D. W. O. Rogers, F. Tessier, and B. R. B. Walters. "The EGSnrc Code System: Monte Carlo simulation of electron and photon transport, NRC Technical Report PIRS-701 v4-2-3-2." (Ottawa, 2011).

[14]D. W. O. Rogers, B. Walters, and I. Kawrakow. "BEAMnrc Users Manual, NRC Technical Report PIRS-509(A) rev. L." (Ottawa, 2011).

[15]S. Agostinelli, et al. "Geant4 – A simulation toolkit." Nucl. Instrum. Meth. A **506**, 250–303 (2003).

[16]J. Allison, et al. "Geant4 Developments and Applications." IEEE Trans. Nucl. Sci. **53**, 270–278 (2006).

[17]D. B. Pelowitz, J. S. Hendricks, J. W. Durkee, M. R. James, M. L. Fensin, G. W. McKinney, S. G. Mashnik, and L. S. Waters. "MCNPX 2.7.A Extensions – Report LA-UR-08-07182." (Los Alamos, New Mexico, 2008).

[18]J. Sempau, E. Acosta, J. Baro, J. M. Fernández-Varea, and F. Salvat. "An algorithm for Monte Carlo simulation of coupled electron-photon transport." Nuclear Instruments and Methods in Physics Research Section B: Beam Interactions with Materials and Atoms **132**, 377–390 (1997).

[19]F. Salvat, J. M. Fernández-Varea, and J. Sempau. "PENELOPE-2011: A Code System for Monte Carlo Simulation of Electron and Photon Transport." (OECD-NEA, Issy-les-Moulineaux, France, 2011). (Available in PDF at http://www.oecd-nea.org/lists/penelope.html.)

[20]J. Sempau, A. Badal, and L. Brualla. "A PENELOPE-based system for the automated Monte Carlo simulation of clinacs and voxelized geometries-application to far-from-axis fields." Med. Phys. **38**, 5887–5895 (2011).

[21]J. H. Hubbell and S. M. Seltzer. "Tables of X-Ray Mass Attenuation Coefficients and Mass Energy-Absorption Coefficients from 1 keV to 20 MeV for Elements Z = 1 to 92 and 48 Additional Substances of Dosimetric Interest." July 2004 [accessed December 2007]. (Available from http://physics.nist.gov/PhysRefData/XrayMassCoef/cover.html.)

[22]International Commission on Radiation Units and Measurements. *ICRU Report 46: Photon, electron, proton, and neutron interaction data for body tissues*. International Commission on Radiation Units and Measurements, Bethesda, MD, 1992.

[23]G. R. Hammerstein, D. W. Miller, D. R. White, M. E. Masterson, H. Q. Woodard, and J. S. Laughlin. "Absorbed radiation dose in mammography." Radiology **130**, 485–491 (1979).

[24]K. Cranley, B. J. Gilmore, G. W. A. Fogarty, and L. Desponds. "Catalogue of diagnostic x-ray spectra and other data." Report No. 78. Institute of Physics and Engineering in Medicine, York, 1997.

[25]International Electrotechnical Commission. "IEC 61267 – Medical diagnostic x-ray equipment—radiation conditions for use in the determination of characteristics." Geneva, Switzerland, 2005.

[26]J. M. Boone. "Glandular breast dose for monoenergetic and high-energy X-ray beams: Monte Carlo assessment." Radiology **213**, 23–37 (1999).

[27]J. M. Boone, T. R. Fewell, and R. J. Jennings. "Molybdenum, rhodium, and tungsten anode spectral models using interpolating polynomials with application to mammography." Med. Phys. **24**, 1863–1874 (1997).

[28]R. Ribberfors. "Relationship of the relativistic Compton cross section to the momentum distribution of bound electron states." Physical Review B **12**, 2067–2074 (1975).

[29]F. Biggs, L. B. Mendelsohn, and J. B. Mann. "Hartree-Fock Compton profiles for the elements." Atomic Data and Nuclear Data Tables **16**, 201–309 (1975).

[30]D. Brusa, G. Stutz, J. A. Riveros, J. M. Fernández-Varea, and F. Salvat. "Fast sampling algorithm for the simulation of photon Compton scattering." Nucl. Instrum. Meth. A **379**, 167–175 (1996).

[31]E. S. M. Ali. "Appendix C: Refining NIST XCOM photon cross sections in EGSnrc." In *Accurate unfolding of photon spectra of clinical linear accelerators using transmission measurements.* Ph.D. thesis, Carleton University, Ottawa, 2012.

[32]D. Bote and F. Salvat. "Calculations of inner-shell ionization by electron impact with the distorted-wave and plane-wave Born approximations." Physical Review A **77**, 042701 (2008).

[33]I. Kawrakow, D. W. Rogers, and B. R. Walters. "Large efficiency improvements in BEAMnrc using directional bremsstrahlung splitting." Med. Phys. **31**, 2883–2898 (2004).

[34]E. Mainegra-Hing and I. Kawrakow. "Efficient x-ray tube simulations." Med. Phys. **33**, 2683–2690 (2006).

[35]B. R. B. Walters, I. Kawrakow, and D. W. O. Rogers. "History by history statistical estimators in the BEAM code system." Med. Phys. **29**, 2745–2752 (2002).

[36]J. Sempau, A. Sánchez-Reyes, F. Salvat, H. O. b. Tahar, S. B. Jiang, and J. M. Fernández-Varea. "Monte Carlo simulation of electron beams from an accelerator head using PENELOPE." Phys. Med. Biol. **46**, 1163 (2001).

[37]J. H. Hubbell, W. J. Veigele, E. A. Briggs, R. T. Brown, D. T. Cromer, and R. J. Howerton. "Atomic form factors, incoherent scattering functions, and photon scattering cross sections." Journal of Physical and Chemical Reference Data **4**, 471–538 (1975).